

**Understanding the impact of alloying elements on elastic
constants of L1₂ structured Nickel-based superalloys :**

A combined first principle and machine learning approach

Dissertation

Submitted in partial fulfilment of the

Requirements of Degree of

Master of Technology

In

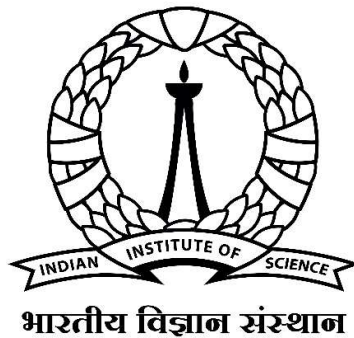
Materials Engineering

By

Zaif Mohammed

Under the guidance of

Prof. S. Karthikeyan



Department of Materials Engineering,

Indian Institute of Science,

Bangalore-560012, India.

June 2023

Abstract

This study focuses on investigating the impact of alloying elements, such as Germanium (Ge), Silicon (Si), and Aluminium (Al), on the elastic properties of L1₂ structured Nickel (Ni)-based superalloys. To analyze these effects, first-principle density functional theory (DFT) calculations were performed using the generalized gradient approximation.

The supercell employed in the calculations consisted of 24 Ni atoms along with 8 Al, 8 Ge and 8 Si atoms, which results in the formation of the L1₂ structures of 32 atoms of Ni₃Al, Ni₃Ge and Ni₃Si respectively. To explore the influence of Si, Ge and Al, substitutions of these atoms were made in the X sublattice of Ni₃X where X = (Al, Ge, Si), resulting in different intermediate compositions of L1₂ structures. These compositions are denoted as Ni₃Al_(1-x)Ge_x, Ni₃Ge_(1-x)Si_x and Ni₃Si_(1-x)Ge_x.

The objective of this research is to develop a machine-learning (ML) model capable of predicting the elastic properties of the intermediate compositions in Ni₃Al_(1-x-y)Ge_xSi_y systems, as well as for the aforementioned intermediate compositions of L1₂ structures. The ML models are trained using a feature set derived from the fingerprints of the L1₂ structured pseudo-binary alloy configurations. These fingerprints are obtained through radial distribution calculations, which provide information of nearest neighbours of bond types of Al-Al, Al-Ge, Al-Si, Si-Si, Si- within the configurations.

By leveraging the ML models trained on the feature set, this research aims to accurately predict the elastic properties of the intermediate compositions of interest. This predictive capability enables a deeper understanding of the effects of alloying elements on the elastic properties of L1₂ structures in Nickel-based superalloys, facilitating the design and development of advanced materials with desired mechanical characteristics.

Contents

Abstract	ii
List of Figures.....	v
List of Tables	vi
Chapter 1	1
Background.....	1
1.1 Introduction	1
1.2 Approach of this work.....	2
1.3 Density Functional Theory	2
Chapter 2	5
Methodology	5
2.1 Optimization and validation	5
2.2 Supercell construction.....	6
2.3 Bulk property calculation.....	7
2.3.1 Lattice parameter.....	7
2.3.2 Cohesive energy	7
2.3.3 Elastic constants calculation	7
2.4 Hill averaging method	9
2.4.1 Voigt average.....	10
2.4.2 Reuss average	10
2.4.3 Hill average	10
Chapter 3	12
Results and discussions of the DFT predicted data.....	12
3.1 Bulk properties of Ni₃Al.....	12
3.1.1 Effect of Ge on bulk properties of Ni₃Al_(1-x)Ge_x.....	12
3.1.2 Effect of Ge on elastic constants of Ni₃Al_(1-x)Ge_x.....	13
3.1.3 Effect of Ge on mechanical properties (Bulk, Shear, Young's modulus) of Ni₃Al_(1-x)Ge_x ...	16
3.1.4 Effect of Ge on anisotropy ratio of Ni₃Al_(1-x)Ge_x	18
3.2 Bulk properties of Ni₃Si	19
3.2.1 Effect of Si on bulk properties of Ni₃Al_(1-x)Si_x	19
3.2.2 Effect of Si on elastic constants of Ni₃Al_(1-x)Si_x	20
3.2.3 Effect of Si on mechanical properties (Bulk, Shear and Young's modulus) of Ni₃Al_(1-x)Si_x	21
3.2.4 Effect of Si on anisotropy ratio of Ni₃Al_(1-x)Si_x	23
3.3 Bulk properties of Ni₃Ge	24
3.3.1 Effect of Si on bulk properties of Ni₃Ge_(1-x)Si_x	24
3.3.2 Effect of Si on elastic constants of Ni₃Ge_(1-x)Si_x	25

3.3.3 Effect of Si on mechanical properties (Bulk, Shear and Young's modulus) of $\text{Ni}_3\text{Ge}_{(1-x)}\text{Si}_x$	26
3.3.4 Effect of Si on anisotropy ratio of $\text{Ni}_3\text{Ge}_{(1-x)}\text{Si}_x$	28
Chapter 4	30
Descriptors of the configurations	30
4.1 Feature selection	30
4.2 ML model selection	32
4.3 ML-NN model training and testing	33
Chapter 5	34
Results and discussions of ML-NN predicted data	34
5.1 Developing and interpreting neural networks using TensorFlow for result analysis.	40
Chapter 6	44
Validation the developed neural networks model	44
6.1 Validating on intermediate compositions of ternary phase diagram of $\text{Ni}_3\text{Al}_{(1-x-y)}\text{Ge}_x\text{Si}_y$	44
Chapter 7	49
Conclusion	49
References	50
Appendix	52
Optimization	52

List of Figures

Figure 1: Effect of increase in Ge content on bulk properties of $\text{Ni}_3\text{Al}_{(1-x)}\text{Ge}_x$	13
Figure 2: Effect of increase in Ge on elastic constants (C_{11} , C_{12} , C_{44}) of $\text{Ni}_3\text{Al}_{(1-x)}\text{Ge}_x$	15
Figure 3: Effect of Increase in Ge content on mechanical properties (Bulk, Shear, Young's modulus) of $\text{Ni}_3\text{Al}_{(1-x)}\text{Ge}_x$	17
Figure 4: Effect of increase in Ge content on anisotropy ratio of $\text{Ni}_3\text{Al}_{(1-x)}\text{Ge}_x$	18
Figure 5: Effect of increase in Si content on bulk properties of $\text{Ni}_3\text{Al}_{(1-x)}\text{Si}_x$	20
Figure 6: Effect of increase in Si content on elastic constants (C_{11} , C_{12} , C_{44}) of $\text{Ni}_3\text{Al}_{(1-x)}\text{Si}_x$	21
Figure 7: Effect of increase in Si content on mechanical properties (Bulk, Shear, Young's modulus) of $\text{Ni}_3\text{Al}_{(1-x)}\text{Si}_x$	22
Figure 8: Effect of increase in Si content on anisotropy ratio of $\text{Ni}_3\text{Al}_{(1-x)}\text{Si}_x$	23
Figure 9: Effect of increase in Si content on bulk properties of $\text{Ni}_3\text{Ge}_{(1-x)}\text{Si}_x$	25
Figure 10: Effect of increase in Si content on elastic constants (C_{11} , C_{12} , C_{44}) of $\text{Ni}_3\text{Ge}_{(1-x)}\text{Si}_x$	26
Figure 11: Effect of increase in Si content on mechanical properties (Bulk, Shear, Young's modulus) of $\text{Ni}_3\text{Ge}_{(1-x)}\text{Si}_x$	27
Figure 12: Effect of increase in Si content on anisotropy ratio of $\text{Ni}_3\text{Ge}_{(1-x)}\text{Si}_x$	28
Figure 13: Bar plot represents the number of 1 st ,2 nd ,3 rd nearest neighbour bonds of type Si-Si, Si-Ge, Ge-Ge in $\text{Ni}_3\text{Ge}_{0.25}\text{Si}_{0.375}$ configuration.	31
Figure 14: Pair plot grid comparing the C_{ij} constants predicted by the neural networks model against the ones calculated using DFT. The training and test sets consisted of 75% and 25% of the data respectively.....	41
Figure 15: Pair plot grid comparing the C_{ij} constants predicted by the neural networks model against the ones calculated using DFT. The training and test sets consisted of 50% and 50% of the data respectively.....	42
Figure 16: Contour plot comparing convergence of E-cut off vs K-spacing for the optimal cohesive energy of relaxed volume of Ni_3Al	52
Figure 17:Contour plot comparing convergence of E-cut off vs K-spacing for the optimal lattice parameter of relaxed volume of Ni_3Al	52
Figure 18: Contour plot comparing convergence of E-cut off vs K-spacing for the optimal computational time of relaxed volume of Ni_3Al	53
Figure 19: line plot comparing smearing width convergence w.r.t to cohesive energy and computational cost of Ni_3Al	53

List of Tables

Table 1: Calculated bulk properties of Ni ₃ Al and its comparison with experimental values.....	12
Table 2: Calculated bulk properties and elastic constants for different compositions of Ni ₃ Al _(1-x) Ge _x . ..	18
Table 3: Bulk properties for Ni ₃ Si and its comparison with experimental values.....	19
Table 4: Calculated bulk properties and elastic constants for different compositions of Ni ₃ Al _(1-x) Si _x ..	24
Table 5: Bulk properties for Ni ₃ Ge and its comparison with experimental values.....	24
Table 6: Calculated bulk properties and elastic constants for different compositions of Ni ₃ Ge _(1-x) Si _x ..	29
Table 7: First nearest neighbours up to 3 of bond types of Al-Al, Si-Al, Si-Si, Ge-Al, Si-Ge, Ge-Ge in Ni ₃ Al _(1-x) Ge _x compositions and it's different configurations.....	34
Table 8: Nine different DFT simulated elastic constants (in Gpa) for the compositions of Ni ₃ Al _(1-x) Ge _x	35
Table 9: First nearest neighbours up to 3 of bond types of Al-Al, Si-Al, Si-Si, Ge-Al, Si-Ge, Ge-Ge in Ni ₃ Al _(1-x) Si _x compositions and it's different configurations	36
Table 10: Nine different DFT simulated elastic constants (in Gpa) for the compositions of Ni ₃ Al _(1-x) Si _x	37
Table 11: First nearest neighbours up to 3 of bond types of Al-Al, Si-Al, Si-Si, Ge-Al, Si-Ge, Ge-Ge in Ni ₃ Ge _(1-x) Si _x compositions and it's different configurations.	38
Table 12: Nine different DFT simulated elastic constants (in Gpa) for the compositions of Ni ₃ Ge _(1-x) Si _x	39
Table 13: 15 different compositional configurations of Nickel-based pseudo-ternary alloys on which NN model is validated.....	44
Table 14: Comparison of DFT simulated and ML model predicted 9 different elastic constants(in Gpa) with margin of errors for compositional configurations of Ni ₃ Al _{0.725} Ge _{0.125} Si _{0.125}	45
Table 15: Comparison of DFT simulated and ML model predicted 9 different elastic constants(in Gpa) with margin of errors for compositional configurations of Ni ₃ Al _{0.25} Ge _{0.375} Si _{0.375}	46
Table 16: Comparison of DFT simulated and ML model predicted 9 different elastic constants(in Gpa) with margin of errors for compositional configurations of Ni ₃ Al _{0.375} Ge _{0.375} Si _{0.25}	47
Table 17: Comparison of DFT simulated and ML model predicted 9 different elastic constants(in Gpa) with margin of errors for compositional configurations of Ni ₃ Al _{0.25} Ge _{0.5} Si _{0.25}	48

Chapter 1

Background

1.1 Introduction

- Significance of Ni-Al Alloys and application of machine learning in predicting mechanical properties. Ni-Al alloys, particularly Ni-Al single crystal alloys, have found widespread use in both civilian and military applications due to their exceptional attributes such as high strength, stability at high temperatures, and resistance to corrosion and oxidation in aggressive environments. Among the various Ni-Al alloys, the L₁₂-ordered Ni₃Al-based single crystal alloys have garnered significant attention as superalloys, primarily due to their remarkable mechanical properties at elevated temperatures. These alloys have been extensively employed in the production of hot components for gas turbines.
- Ni₃Al, classified as an intermetallic compound, exhibits valuable mechanical properties, including elastic modulus, bulk modulus, and shear modulus, which have been extensively investigated through experimental techniques. However, the discrete nature of experimental data arises from variations in material preparation, processing, and testing methods. To overcome the limitations imposed by experimental approaches, first-principles calculations have gained prominence in recent years for accurately determining the elastic properties of alloys and intermetallic compounds.
- This thesis aims to explore the mechanical parameters, such as bulk modulus, shear modulus, and Young's modulus, of Ni₃Al, as well as its alloys with Ni₃Si and Ni₃Ge. Additionally, the investigation encompasses the intermediate compositions present in the ternary phase diagram of these systems, achieved by incorporating alloying elements such as aluminium (Al), silicon (Si), and germanium (Ge). Furthermore, the impact of alloying on lattice parameters and cohesive energy will be examined. To predict the mechanical properties with enhanced accuracy, machine learning models will be developed and employed in this study.
- By combining the power of computational calculations, data analysis, and machine learning techniques, this research aims to provide valuable insights into the mechanical properties of Ni-Al-based alloys. The integration of these approaches not only complements traditional experimental methods but also expands the understanding of the relationships between alloy composition, mechanical behaviour, contributing to the development of advanced materials with optimized properties for various applications.

1.2 Approach of this work

- Evaluating Mechanical Properties of Pseudo-Binary Alloys using First-Principles Calculations
- In this study, we employ first-principles electronic structure calculations based on Density Functional Theory (DFT) to determine the lattice parameters, cohesive energies, and elastic constants (C_{ij}) of pseudo-binary alloys. Specifically, we investigate the $Ni_3Al_{(1-x)}Si_x$, $Ni_3Al_{(1-x)}Ge_x$, and $Ni_3Ge_{(1-x)}Si_x$ systems, which exhibit various compositions.
- The DFT approach is widely utilized in the fields of physics, chemistry, material science, and engineering for modeling and studying diverse materials. By describing the interacting system of electrons in terms of their density rather than many-body wave functions, DFT provides an efficient means of determining the ground state properties of atoms, molecules, and condensed phases.
- Using DFT, we calculate the electronic structure and properties of the pseudo-binary alloys, allowing us to derive their lattice parameters, cohesive energies, and elastic constants. These elastic constants, namely C_{ij} , serve as crucial inputs for the evaluation of several mechanical properties, including the bulk modulus, shear modulus, and Young's modulus. We utilize the Hill Averaging method to calculate these mechanical properties based on the obtained elastic constants.
- By employing this approach, we aim to gain a comprehensive understanding of the mechanical behaviour and properties of the investigated pseudo-binary alloys. The utilization of first-principles calculations and the derived mechanical properties will contribute to the characterization and prediction of the alloys' performance, enabling the design and development of novel materials with tailored properties for various engineering applications.

1.3 Density Functional Theory

- The electronic and geometrical structure of a system can be predicted by solving the quantum mechanical equation of state. The fundamental unit of the quantum theory is the Hamiltonian of the ion-electron system, which is functional of the nuclear and electronic coordinates. The simplest quantum-mechanical equation is the single electron Schrodinger time-independent equation [18].

$$-\left[\frac{\hbar^2}{2m}\nabla^2 + V\right]\psi = E\psi \quad (1)$$

- The complexity of the Hamiltonian increases with the number of electrons in the system. The first step in simplifying this equation is the adiabatic or Born-Oppenheimer approximation. Here the Hamiltonian is freed of the kinetic energy of the nuclei. Since the force acting on both particles are same, the instantaneous velocity of electrons is

much larger than the nuclei. Hence, the nuclei can be assumed to be motionless in the time the electron takes to reach its ground state. The Hamiltonian contains the kinetic energy of the electrons, energy due to the interaction of the electrons with the ions and energy due to interactions of the electrons themselves. Electron-electron repulsion is represented by a Mean-Field approximation in which an electron interacts with an average potential created by an electron gas of constant density. In doing so, an exchange term is needed to account for Pauli's exclusion principle, according to which two electrons with the same spin cannot be in the same quantum state. The many-electron Hamiltonian is further reduced to one electron problem by Density Functional Theory. Based on the Hohenberg-Kohn theorem, wherein the electronic wavefunction is described by corresponding spatially varying electronic density. The result of this theorem is that the total energy of the system becomes a unique function of the electronic density distribution, which is a measurable quantity. The energy has its minimum value at the ground state electron density [18]. The Hamiltonian then becomes

$$\left[-\frac{\hbar^2}{8m\pi^2} \frac{\partial^2}{\partial \vec{r}^2} + V_{el-ion} + e^2 \int \frac{n(\vec{r}')}{\vec{r}-\vec{r}'} d\vec{r}' + V_{xc}(\vec{r}) \right] \psi(\vec{r}) = \epsilon_i \psi_i(\vec{r}) \quad (2)$$

Where,

$$n(\vec{r}) = \sum_{i=1}^n \psi_i(\vec{r}) \quad (3)$$

$$V_{xc}(\vec{r}) = \frac{\partial E_{xc}[n(\vec{r})]}{\partial n(\vec{r})} \quad (4)$$

- This exchange-correlation energy is approximated by Generalised Gradient Approximation (GGA).
- In GGA, the E_{xc} of an electron at a position depends not only on its local electron density but also on the gradient of electron density. In this sense, the spatial distribution of electron density is accounted for. As a result, superior structural properties and ground-state energies are achieved using the GGA approximation.
- The Wavefunction itself can be described by a finite linear combination of single electron wavefunctions called the basis functions. The advantage of using a plane wave basis set is that it is sufficiently smooth when away from the atomic positions and near the atoms, it is strongly fluctuates with radial distance—addressed by pseudo potential approximation, where electrons are divided in two groups: valence and Inner core. In this approximation, the decoupling of core and valence electrons allows for the screening of fluctuations of the plane wave near the core of the atom. The approximation is physically valid in most cases; electron in the inner shells is strongly bound and do not play a significant role in the chemical binding of atoms, thus forming with nucleus an almost Inert core. Binding properties are almost completely due to the valence electrons, especially in metals and semiconductors. So, while pseudo potentials work fine for s or p-bonded metals, it has limitations when d and f orbitals come into play. In that case, ultra-soft pseudopotentials are used. In the case of the LPAW method, the space near the atom is approximated by

using spherical waves. These spherical waves are so chosen that they maintain their continuity with the plane's waves when away from the atom.

- Thus, after defining all the necessary elements, the Hamiltonian can now be described as:

$$F[n(\vec{r})] = T_s[n(\vec{r})] + E_H[n(\vec{r})] + E_{xc}[n(\vec{r})] \quad (5)$$

- Whereas in eq 5, T_s is the kinetic energy term, E_H is the external potential, and E_{xc} is the exchange-correlation functional. Thus, the ground state energy of the system can be evaluated recursively or self-consistently.
- The advantage of the ab-initio method is that it generally stems from the fact that the electronic structure information is present here. So, ab-initio methods do not depend on any empirical function or other material-dependent properties. This makes the results obtained through ab-initio methods highly accurate.

Chapter 2

Methodology

- Electronic structure calculation and convergence criteria.
- To perform electronic structure calculations, we utilized the Vienna Ab-initio Simulation Package (VASP) software. Within VASP, we employed the Project Augmented Wave (PAW) method, which is an extension of the LAPW pseudo-potential approach, to define the basis set for our calculations. This method enables us to accurately describe the electronic structure of the materials under investigation.
- For the exchange-correlation energy function, we employed the Generalized Gradient Approximation with Perdew-Burke-Ernzerhof (GGA-PBE) parameterization. This approximation accounts for the effects of electron-electron interactions and provides a reliable description of the electronic properties of the materials.
- All calculations were performed at a temperature of 0 K, allowing us to focus solely on the intrinsic properties of the systems. To ensure convergence and accuracy of the results, we systematically adjusted various parameters. The cut-off energy, k-points, and the smearing width parameters were carefully tuned to achieve convergence within a specified percentage. Specifically, we aimed to match the lattice parameters and cohesive energy of the investigated systems with experimental data to a desired degree of accuracy.
- Furthermore, we performed elastic constants calculations for different configurations of $\text{Ni}_3\text{Al}_{(1-x)}\text{Ge}_x$, $\text{Ni}_3\text{Ge}_{(1-x)}\text{Si}_x$, $\text{Ni}_3\text{Si}_{(1-x)}\text{Al}_x$, and intermediate compositions. By refining the aforementioned parameters, we sought to obtain reliable and precise elastic constants that describe the mechanical behaviour of these materials.
- The rigorous optimization of the computational parameters and convergence criteria in our calculations ensures that our results are robust and consistent. This methodology allows us to accurately assess the mechanical properties of the materials, providing valuable insights into their behaviour and enabling the prediction and design of new materials with tailored properties for various applications.

2.1 Optimization and validation

- To ensure good and efficient calculations, we performed optimization procedures for the plane wave energy cut-off, k-point grid, and smearing width parameters. Initially, we conducted these optimizations for the Ni_3Al system, and the resulting optimized values were subsequently used for calculations involving Ni_3Ge , Ni_3Si , and intermediate compositions.
- In order to validate the reliability of our simulation methodology, we compared the calculated results of lattice parameters, cohesive energies, and elastic constants (excluding intermediate compositions) with available literature data. This comparison served as a benchmark to assess the excellent and consistency of our simulation approach.

- For all calculations, we employed a plane wave energy cut-off of 450 eV. This cut-off value determines the level of accuracy in representing the electronic wave functions and influences the precision of the calculated properties.
- The k-point grid, which is a discretized sampling of the Brillouin zone, was optimized to obtain good results while minimizing computational cost. The optimum k-point grid size used in our calculations was determined to be 5 grid points.
- In terms of the smearing technique, we utilized the Methfessel-Paxton integration scheme with a smearing width of 0.12 eV. This smearing width accounts for the thermal broadening of electronic occupations and enables the calculation of properties at finite temperatures.
- By adopting these optimization procedures, we aimed to obtain reasonably good results without compromising computational efficiency. This ensures that our calculations provide reliable insights into the structural, energetic, and mechanical properties of the studied systems, facilitating their characterization and exploration for potential applications.

2.2 Supercell construction

- To investigate the properties of $\text{Ni}_3\text{Al}_{(1-x)}\text{Ge}_x$, $\text{Ni}_3\text{Ge}_{(1-x)}\text{Si}_x$, $\text{Ni}_3\text{Si}_{(1-x)}\text{Al}_x$ alloys, we employed a supercell approach based on the L1₂ crystal structure. The L1₂ structure consists of two distinct sub-lattices: an A sublattice located at the face centres, primarily containing Ni atoms, and a B sublattice situated at the corners, where Al, Si, and Ge atoms are doped depending on the specific alloy system.
- For the calculation of intermediate compositions, we constructed supercells containing 32 atoms. These supercells were then subjected to structural relaxation using an energy minimization technique. In this process, we minimized the total energy of the system by adjusting the lattice parameters, allowing the atoms to find their most energetically favourable positions.
- During the structural relaxation, the lattice parameters were varied to achieve a pressure below 10 Mpa within the systems. This criterion ensured that the systems were at equilibrium and allowed us to determine the corresponding equilibrium lattice parameters and cohesive energies.
- By employing the supercell construction and subsequent structural relaxation, we were able to accurately describe the atomic arrangements and optimize the energetics of the alloys. This approach enabled us to investigate the influence of different compositions on the lattice parameters and cohesive energies, providing valuable insights into the structural properties and stability of the studied systems.

2.3 Bulk property calculation

2.3.1 Lattice parameter

- To determine the equilibrium lattice parameter and achieve a pressure below 10 Mpa, we systematically varied the lattice parameter in steps of 0.001Å. Through this iterative process, we observed that even a small change of 0.001Å in the lattice parameter could result in a pressure shift of approximately 15 Mpa within the system.
- By repeating the calculations and carefully interpolating between the lattice parameter values and their corresponding pressures, we identified the lattice parameter at which the pressure reached 0 Mpa or fell below the desired threshold of 10 Mpa. This approach allowed us to obtain precise lattice parameters that ensured the systems were at equilibrium, with minimal internal stress.
- By determining the equilibrium lattice parameter, we could confidently assess the structural properties and behaviour of the alloys under investigation.

2.3.2 Cohesive energy

- The cohesive energy, which represents the energy difference between atoms in a bonded (crystalline) state and their isolated gaseous state, was determined in this study. To calculate the cohesive energy, we evaluated the energies of isolated atoms by placing them in a large supercell with dimensions of approximately 13Å. It is important to note that the bonded state can have a crystal structure that may not necessarily be its most stable configuration.
- In this work, the cohesive energies of both pure elements and alloy compositions were computed using a specific formula [4]:

$$E_c(Ni_3X_{(1-x)}Y_x) = E(Ni_3X_{(1-x)}Y_x) - 3E_{iso}(Ni) - (1-x)E_{iso}(X) - xE_{iso}(Y) \quad (6)$$

- Where E_c and E are the cohesive and bulk energies of $Ni_3X_{(1-x)}Y_x$, E_{iso} is the energy of an isolated atom in a large supercell.

2.3.3 Elastic constants calculation

- The elastic constants (C_{11} , C_{12} , C_{44}) of Ni₃Al, Ni₃Ge, Ni₃Si, and the intermediate compositions were determined to investigate their mechanical properties. The influence of alloying on the moduli in pseudo-binary systems was also examined. To derive the bulk modulus, shear modulus, and Young's modulus, the elastic constants were utilized in the Hill Averaging method.
- Matrix notation for elasticity is given by [4].

$$\sigma_i = \sum_{j=1}^6 C_{ij} \varepsilon_j \quad (7)$$

Where, σ_i is the stress tensor, ε_j is the strain tensor, and C_{ij} is the stiffness tensor. There are two ways of extracting elastic data through ab initio calculations.

- i. Analysis of total energy of properly strained states of materials.
- ii. Analysis of changes in the calculated stress values resulting from changes in strain.

- In this project, a second approach was employed to calculate the elastic moduli, which involved analyzing the changes in stress resulting from changes in strain. These two quantities are related through the stiffness constants. The "MT elastic properties" module of Medea, in combination with VASP, was utilized to implement this technique. Elastic constants were determined using a symmetry-general least-square extraction method. Strains below 5% were imposed on three to four different configurations for each composition to explore the effects of alloying. From the resulting data, a weighted average of the moduli was obtained by considering all individual configurations, and the average modulus was reported as the elastic constant. The quasi-random distribution of alloying additions in the supercell disrupts the cubic symmetry, which was addressed by employing an averaging scheme proposed by (Kim et al., 2010; Wu & Li, 2012a)[16-17]. For each configuration, the average elastic constants (C_{ij}) were evaluated using the following procedure:

Stiffness:

$$\overline{C_{11}} = (C_{11} + C_{22} + C_{33})/3 \quad (8)$$

$$\overline{C_{12}} = (C_{12} + C_{13} + C_{23})/3 \quad (9)$$

$$\overline{C_{44}} = (C_{44} + C_{55} + C_{66})/3 \quad (10)$$

Compliances:

$$S_{11} = (C_{11} + C_{12})/(C_{11} - C_{12})(C_{11} + 2C_{12}) \quad (11)$$

$$S_{11} = (-C_{12})/(C_{11} - C_{12})(C_{11} + 2C_{12}) \quad (12)$$

$$S_{44} = 1/C_{44} \quad (13)$$

$$\overline{S_{11}} = (S_{11} + S_{22} + S_{33})/3 \quad (14)$$

$$\overline{S_{12}} = (S_{12} + S_{13} + S_{23})/3 \quad (15)$$

$$\overline{S_{44}} = (S_{44} + S_{55} + S_{66})/3 \quad (16)$$

- For each composition, they are subsequent configurations are present and due to the change in symmetry from cubic to primitive in the 32-atom simulation box, the 9 elastic constants associated with cubic symmetry are averaged to obtain 3 elastic constants $\overline{C_{11}}, \overline{C_{12}}, \overline{C_{44}}$
- Taking $\text{Ni}_3\text{Al}_{0.5}\text{Ge}_{0.5}$ as an example, there are a total of six distinct configurations possible for this composition. Elastic constants (C_{ij}) were determined for each of these six configurations using the aforementioned method. The calculated values were then

used to compute weighted average values, where the weighting factor was determined by the probability of finding each configuration. These weighted average values of the elastic constants were subsequently reported.

Errors in elastic constant estimation arise from three sources:

1. The least-square fit error for determination of individual C_{ij} for each configuration.
2. Averaging to determine \overline{C}_{ij}
3. Weighted averaging over various configurations to determine the reported C_{ij} for the composition.

These errors were estimated, and it was found that least square fit errors and differences between configurations dominated the errors, and they were in range of 10-40 Mpa.

2.4 Hill averaging method

- In order to calculate the mechanical properties of a cubic crystal system, such as the Bulk modulus, Shear modulus, and Young's modulus, we rely on the elastic constants. These elastic constants provide important information about the material's response to stress and strain.
- For a cubic crystal system, there are three independent elastic constants: C_{11} , C_{12} , and C_{44} . These constants are determined based on the symmetry of the stress and strain tensors, as well as other principles such as the strain energy constant and Neumann's principle. The Voigt 2-index notation is commonly used to represent these elastic constants.
- When considering a polycrystalline alloy, the relative elastic constants can be derived from the single-crystal elastic constants. This is done by considering the orientation and alignment of the individual crystalline grains within the polycrystalline material. By taking into account the crystallographic texture and grain boundaries, we can determine the effective elastic constants for the overall material.
- These relative elastic constants provide insight into the mechanical behavior of the polycrystalline alloy, including its ability to withstand stress, deform under strain, and resist deformation. Understanding these properties is crucial for various engineering applications, as it helps in predicting the material's response to external forces and designing structures that can withstand the required loads.

$$\overline{C}_{11} = (C_{11} + C_{22} + C_{33})/3 \quad (17)$$

$$\overline{C}_{12} = (C_{12} + C_{13} + C_{23})/3 \quad (18)$$

$$\overline{C}_{44} = (C_{44} + C_{55} + C_{66})/3 \quad (19)$$

2.4.1 Voigt average

- Under the assumption of iso-strain, different orientations of a material can generate varying stresses, known as effective stiffness. The average isotropic stiffness is obtained by averaging the effective stiffness values across all crystallographic directions [4].

$$\text{Bulk modulus } (B_V) = (\overline{C_{11}} + 2\overline{C_{12}})/3 \quad (20)$$

$$\text{Shear modulus } (G_V) = (\overline{C_{11}} - \overline{C_{12}} + 3\overline{C_{44}})/5 \quad (21)$$

2.4.2 Reuss average

- Under the assumption of iso-stress, different orientations of a material can result in different strains, referred to as effective compliance. The average isotropic compliance is obtained by averaging the effective compliance values across all crystallographic directions [4].

$$\text{Bulk modulus } (B_R) = 1/(3\overline{S_{11}} + 6\overline{S_{12}}) = (\overline{C_{11}} + 2\overline{C_{12}})/3 \quad (22)$$

$$\text{Shear modulus } (G_R) = 5/(4\overline{S_{11}} - 4\overline{S_{12}} + 3\overline{S_{44}}) = 5\overline{C_{44}}(\overline{C_{11}} - \overline{C_{12}})/(4\overline{C_{44}} + 3(\overline{C_{11}} - \overline{C_{12}})) \quad (23)$$

2.4.3 Hill average

- The Hill averaging method is a technique used to estimate the effective mechanical properties of a composite material by taking the average of the Voigt and Reuss bounds. The Voigt bound assumes that all grains in the material are perfectly aligned and share the same strain, while the Reuss bound assumes that each grain is independently strained. By averaging these two bounds, the Hill average provides an approximation of the overall behaviour of the material.
- In the context of elastic constants, the Hill average can be used to calculate the effective bulk modulus, shear modulus, and Young's modulus. The bulk modulus represents the material's resistance to uniform compression, the shear modulus represents its resistance to shear deformation, and Young's modulus represents its stiffness or resistance to linear deformation.
- By considering both the Voigt and Reuss bounds, the Hill average takes into account the different possible loadings and orientations of the composite material, providing a more accurate estimation of its mechanical properties. This approach is particularly useful when dealing with materials that have complex microstructures or contain multiple phases with different elastic properties [4].

$$\text{Bulk modulus } (B_H) = (B_V + B_R)/2 \quad (24)$$

$$\text{Shear modulus } (G_H) = (G_V + G_R)/2 \quad (25)$$

$$\text{Young's modulus } (E_H) = 9B_H G_H / (G_H + 3B_H) \quad (26)$$

- The extent of isotropy or anisotropy in a crystal can be quantified by examining the elastic modulus in all directions. This provides insights into how the material's stiffness varies depending on the orientation. By analyzing the elastic modulus values across different crystallographic directions, we can understand whether the material exhibits isotropic behaviour, where the modulus remains consistent regardless of the direction, or anisotropic behaviour, where the modulus varies significantly depending on the direction.:
$$A = 2C_{44}/(C_{11} - C_{12}) \quad (27)$$

Chapter 3

Results and discussions of the DFT predicted data

3.1 Bulk properties of Ni₃Al

Table 1 presents the bulk properties of Ni₃Al, where the calculated properties are compared with corresponding experimental values for comparison.

Table 1: Calculated bulk properties of Ni₃Al and its comparison with experimental values

	Calculated	Experimental [17]	Error (%)
Lattice parameter (Å)	3.5702	3.57	0.005
Cohesive energy (eV/atom)	4.98	5.23	4.9
C₁₁ (Gpa)	234	230	1.7
C₁₂ (Gpa)	133.5	150	12.3
C₄₄ (Gpa)	129.2	131	1.4
Bulk Modulus (Gpa)	167	177	5.9
Shear Modulus (Gpa)	88.5	85	4.1
Young's Modulus (Gpa)	225.4	219.8	2.5

3.1.1 Effect of Ge on bulk properties of Ni₃Al_(1-x)Ge_x

- Table 2 and Figure 1 present the calculated bulk properties for different compositions of Ni₃Al_(1-x)Ge_x. The focus is on the progressive increase of Ge content in the Ni₃Al alloy, which leads to an increase in the lattice parameter and cohesive energies.
- To elaborate on this, the lattice parameter represents the distance between the crystal lattice points in the material. In this case, as the Ge content increases in the Ni₃Al_(1-x)Ge_x compositions, the lattice parameter progressively increases. This suggests that the incorporation of Ge atoms into the crystal structure of Ni₃Al leads to a larger spacing between the lattice points.
- Additionally, cohesive energy refers to the energy required to completely separate the atoms in a material and is a measure of the stability of the material. In the context of Ni₃Al_(1-x)Ge_x compositions, the cohesive energies are found to increase as the Ge content increases. This implies that the bonding between atoms becomes stronger and more stable with the addition of Ge.
- The above statement emphasizes that the calculated bulk properties, specifically the lattice parameter and cohesive energies, exhibit a consistent trend in response to the progressive increase of Ge in the Ni₃Al alloy. The increasing lattice parameter indicates a larger spacing between lattice points, while the higher cohesive energies reflect stronger bonding and improved stability within the material.

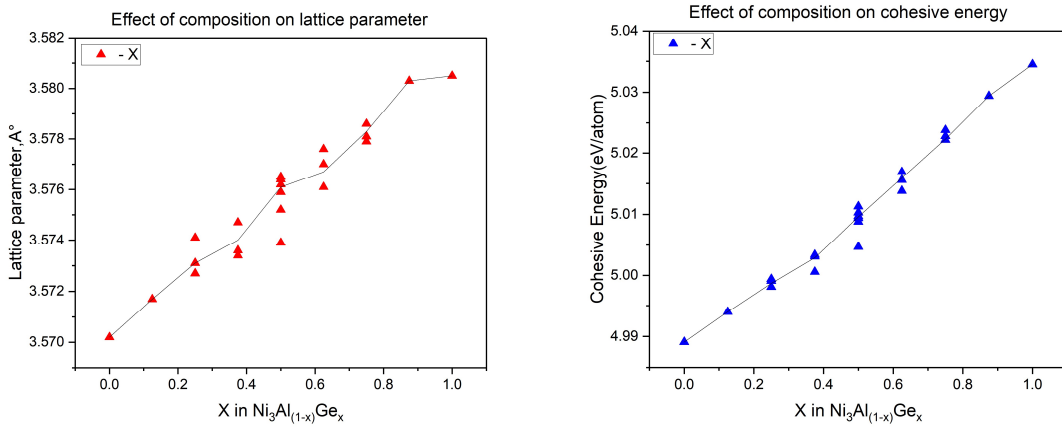


Figure 1: Effect of increase in Ge content on bulk properties of $\text{Ni}_3\text{Al}_{(1-x)}\text{Ge}_x$

3.1.2 Effect of Ge on elastic constants of $\text{Ni}_3\text{Al}_{(1-x)}\text{Ge}_x$

- The calculated elastic constants for different compositions of $\text{Ni}_3\text{Al}_{(1-x)}\text{Ge}_x$ are presented in Table 2 and Figure 2. It further indicates that as the Ge content increases progressively in the $\text{Ni}_3\text{Al}_{(1-x)}\text{Ge}_x$ alloy system, distinct trends are observed for the elastic constants C_{11} , C_{12} , and C_{44} , as shown in Figure 2.
- Elastic constants are parameters that describe the stiffness and mechanical behaviour of a material. C_{11} , C_{12} , and C_{44} are specific elastic constants that correspond to different types of deformation and crystallographic directions in the material.
- The above statement suggests that the addition of Ge to the $\text{Ni}_3\text{Al}_{(1-x)}\text{Ge}_x$ alloy system leads to different trends in the elastic constants C_{11} , C_{12} , and C_{44} . These trends may indicate changes in the stiffness, anisotropy, or other mechanical properties of the alloy as Ge is incorporated.
- To elaborate on this, Figure 2 provides a visual representation of the trends observed for the elastic constants C_{11} , C_{12} , and C_{44} with increasing Ge content. C_{11} represents the stiffness along a specific crystallographic direction, while C_{12} characterizes the stiffness between different crystallographic planes. C_{44} corresponds to the material's resistance to shear deformation along a specific plane.
- From the above statement, it is suggesting that as the Ge content increases progressively, the elastic constants C_{11} , C_{12} , and C_{44} exhibit different trends. These trends may indicate variations in the alloy's stiffness or anisotropy in different crystallographic directions or planes.
- With an increase in Ge content in Ni_3Al , both C_{11} and C_{12} exhibit an increasing trend, while C_{44} shows a decreasing trend. However, there are deviations from the increasing trend in C_{11} at the initial and final compositions. At the initial composition, there is a significant increase, and at the higher end, there is a significant decrease. On the other

hand, C_{12} demonstrates a consistent increase followed by a decrease towards the Al-rich end.

- Both C_{11} and C_{12} display an increasing trend, indicating a rise in the material's resistance to deformation along specific crystallographic directions. This increase suggests that the addition of Ge contributes to strengthening the material. However, deviations from the increasing trend are observed at the initial and final compositions.
- At the initial composition, there is a significant hike in C_{11} , indicating a substantial increase in the material's resistance to deformation along a specific crystallographic direction. This deviation suggests that the addition of a small amount of Ge has a pronounced effect on the material's resistance to deformation, potentially due to changes in atomic arrangement or bonding characteristics.
- Similarly, at the higher end of the Ge content, there is a significant decrease in C_{11} . This lower point indicates a reduced resistance to deformation along a specific crystallographic direction, potentially due to the influence of the higher Ge content or interactions between Ge and other elements in the alloy.
- In contrast to C_{11} , C_{12} demonstrates a consistent increasing followed by decreasing trend as the Ge content increases, implying a continuous enhancement and diminution in the material's resistance to deformation along a different crystallographic direction. However, towards the Al-rich end, C_{12} starts to decrease, suggesting a change in the material's structural and bonding characteristics as the composition becomes richer in Al.
- C_{44} , on the other hand, displays a decreasing trend with increasing Ge content. This indicates a reduction in the material's resistance to shear deformation, potentially resulting from the addition of Ge and its effect on the crystal structure or bonding interactions.
- Interpreting the trends, it can be inferred that the addition of Ge in Ni_3Al compositions significantly influences the elastic constants C_{11} , C_{12} , and C_{44} . The increasing trends in C_{11} and C_{12} suggest that Ge strengthens the material along specific crystallographic directions. The deviations from the increasing trend at the initial and final compositions highlight the non-linear behaviour resulting from the interactions between Ge and the other elements. The decreasing trend in C_{44} indicates a decrease in the material's resistance to shear deformation, potentially due to changes in crystal structure induced by the addition of Ge.

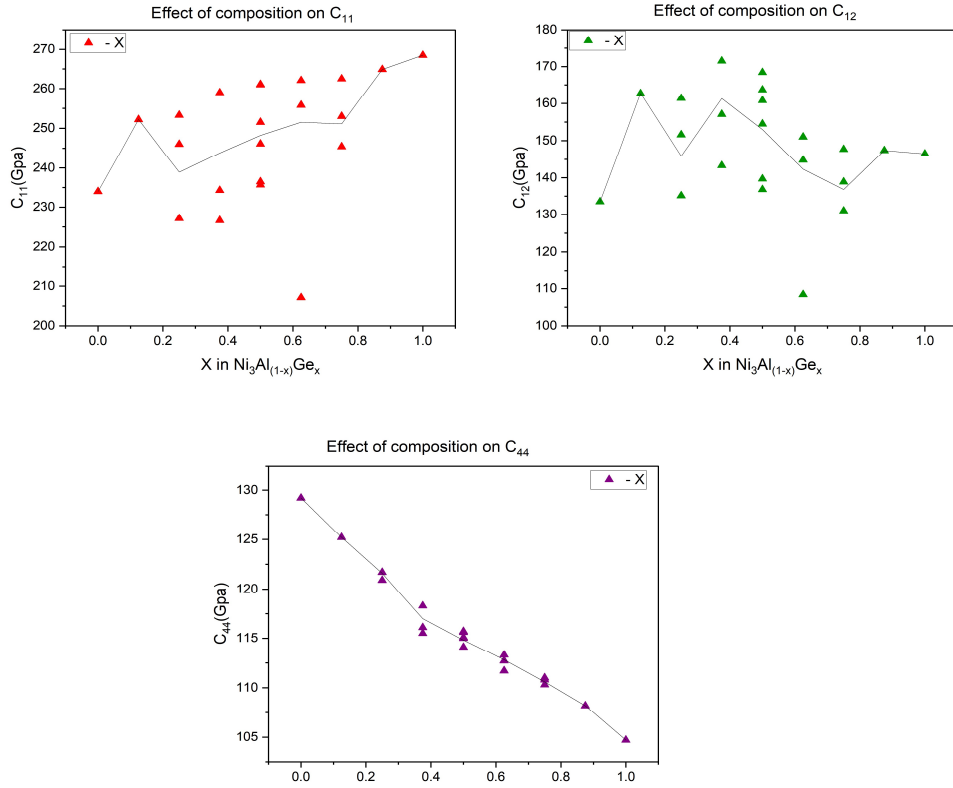


Figure 2: Effect of increase in Ge on elastic constants (C_{11} , C_{12} , C_{44}) of $\text{Ni}_3\text{Al}_{(1-x)}\text{Ge}_x$

- In Figure 2, the presence of different data points at the same compositions indicates the values of various configurations within those compositions. Each data point represents a specific configuration, and these configurations can have different weights or contributions to the overall material's properties. The configurational average weight, depicted as a line at each composition in the figure, represents the average value considering the relative weights of the different configurations.
- To elaborate on this, the composition of $\text{Ni}_3\text{Al}_{(1-x)}\text{Ge}_x$ alloys can have multiple possible atomic arrangements or configurations. These configurations may arise due to the random distribution of atoms or the presence of different crystallographic structures. Each configuration can have its own specific set of elastic constants.
- In Figure 2, the individual data points represent the values of the elastic constants for different configurations at the same compositions. The presence of multiple data points at each composition suggests that the alloy system exhibits configurational variability, leading to variations in the measured elastic constants.
- The configurational average weight, represented by a line at each composition in the figure, indicates the overall weighted average value of the elastic constants, considering the relative importance or prevalence of each configuration. It represents an averaged representation of the elastic constants that accounts for the contributions from different configurations based on their weights.

- The above statement emphasizes that the different configurations within the same compositions of $\text{Ni}_3\text{Al}_{(1-x)}\text{Ge}_x$ alloys have varying weights or contributions to the material's properties. The configurational average weight, as depicted by the line, provides a representative value that considers the influence of different configurations.

3.1.3 Effect of Ge on mechanical properties (Bulk, Shear, Young's modulus) of $\text{Ni}_3\text{Al}_{(1-x)}\text{Ge}_x$

- The calculated mechanical properties of $\text{Ni}_3\text{Al}_{(1-x)}\text{Ge}_x$ compositions, obtained using the Hill averaging method from elastic constants, are presented in Table 2 and Figure 3. It further indicates that the progressive increase of Ge content in the $\text{Ni}_3\text{Al}_{(1-x)}\text{Ge}_x$ alloy system results in different trends for the bulk modulus, shear modulus, and Young's modulus, as depicted in Figure 3.
- Additionally, it is observed that both the shear modulus and Young's modulus of the $\text{Ni}_3\text{Al}_{(1-x)}\text{Ge}_x$ compositions exhibit the same trend with the addition of Ge to the alloy.
- To elaborate on this, the Hill averaging method is a widely used approach to estimate the effective mechanical properties of polycrystalline materials based on their elastic constants. The method considers the anisotropy of individual grains and provides an averaged representation of the material's response.
- In the case of the $\text{Ni}_3\text{Al}_{(1-x)}\text{Ge}_x$ compositions, Figure 3 illustrates the trends observed for the bulk modulus, shear modulus, and Young's modulus as the Ge content increases progressively. The bulk modulus represents a material's resistance to volume change under pressure, while the shear modulus characterizes its resistance to deformation along planes parallel to the applied force. Young's modulus, on the other hand, describes the material's stiffness or resistance to elastic deformation under tension or compression.
- The above sentence implies that the effect of adding Ge to the $\text{Ni}_3\text{Al}_{(1-x)}\text{Ge}_x$ alloy system leads to distinct trends in the bulk modulus, shear modulus, and Young's modulus. These trends may indicate changes in the alloy's mechanical response as a result of Ge incorporation. Furthermore, it suggests that the shear modulus and Young's modulus exhibit similar behaviour with the addition of Ge, implying a correlation between the two mechanical properties.
- Upon increasing the Ge content in Ni_3Al , the Young's modulus initially decreases rapidly, then experiences a sharp increase upon crossing a convex point at compositions below 0.5. The shear modulus follows a similar trend to the Young's modulus, while the bulk modulus displays both increasing and decreasing trends with increasing Ge content.
- Initially, as the Ge content increases, Young's modulus rapidly decreases, indicating a reduction in the material's stiffness. However, upon reaching a certain composition, which is below 0.5, there is a sharp increase in Young's modulus. This convex point represents a critical threshold where the material's stiffness suddenly starts to increase, potentially due to the influence of the added Ge content.
- In contrast, the bulk modulus, which measures the material's resistance to uniform compression, demonstrates both increasing and decreasing trends as the Ge content

increases. This indicates that the compressibility of the material varies with Ge content. The increasing and decreasing trends suggest changes in the material's compressibility at different compositions. However, further analysis is necessary to understand the specific mechanisms responsible for these variations.

- Interpreting the trends, it can be inferred that the addition of Ge content in Ni_3Al compositions significantly influences the mechanical properties, particularly Young's modulus, shear modulus, and bulk modulus. The rapid decrease and subsequent increase of Young's modulus and shear modulus suggest complex interactions between Ge and Al, altering the material's stiffness and resistance to shear deformation. The variations in bulk modulus indicate changes in the material's compressibility, potentially resulting from modifications in the atomic arrangement and bonding characteristics induced by the addition of Ge.

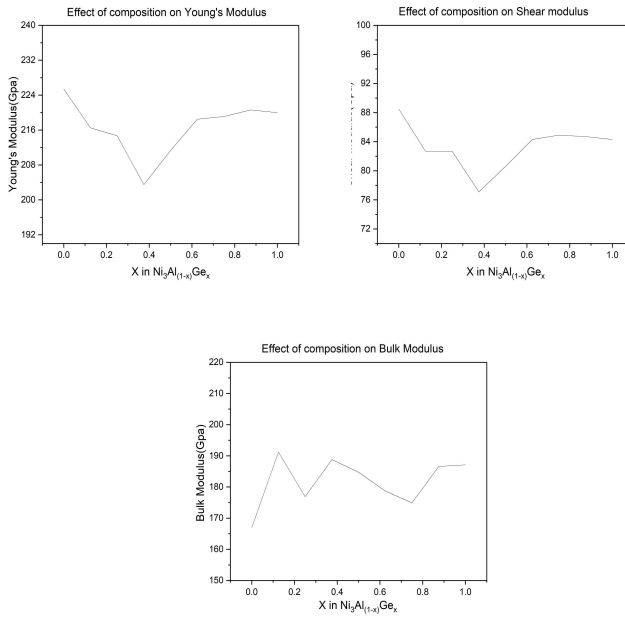


Figure 3: Effect of Increase in Ge content on mechanical properties (Bulk, Shear, Young's modulus) of $\text{Ni}_3\text{Al}_{(1-x)}\text{Ge}_x$

3.1.4 Effect of Ge on anisotropy ratio of $\text{Ni}_3\text{Al}_{(1-x)}\text{Ge}_x$

- The anisotropy ratio refers to the ratio of the magnetic properties (such as magnetization or susceptibility) along different crystallographic directions in a material. Anisotropy can arise due to various factors, including crystal structure, magnetic interactions, and composition.
- In the context of elastic constants, the anisotropy ratio can be quantified using different approaches. One common method is to calculate the ratio between the maximum and minimum values of a specific elastic constant (e.g., Young's modulus or shear modulus) in different crystallographic directions. This ratio provides an indication of the degree of anisotropy in the material's mechanical response.
- It can be inferred that the anisotropy ratio of the elastic constants in the $\text{Ni}_3\text{Al}_{(1-x)}\text{Ge}_x$ compositions decreases as the Ge content (x) increases (Fig 4). This suggests that the mechanical behaviour of the alloy becomes less directionally dependent with a higher Si concentration. It implies that the elastic properties, such as stiffness or deformability, doesn't vary significantly depending on the crystallographic direction in the alloy.

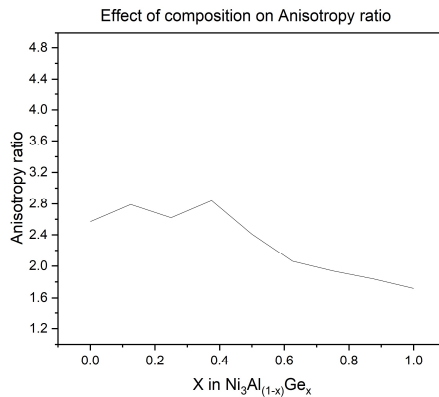


Figure 4: Effect of increase in Ge content on anisotropy ratio of $\text{Ni}_3\text{Al}_{(1-x)}\text{Ge}_x$

Table 2: Calculated bulk properties and elastic constants for different compositions of $\text{Ni}_3\text{Al}_{(1-x)}\text{Ge}_x$

	Lattice parameter (Å)	Cohesive energy (eV/atom)	C_{11} (Gpa)	C_{12} (Gpa)	C_{44} (Gpa)	Bulk Modulus (Gpa)	Shear Modulus (Gpa)	Young's Modulus (Gpa)
Ni₃Al	3.5702	4.9891	234	133.5	129.2	167	88.5	225.4
Ni₃Al_{0.875}Ge_{0.125}	3.5717	4.994	252.2	162.7	125.2	191.2	82.7	216.5
Ni₃Al_{0.75}Ge_{0.25}	3.5731	4.9987	238.9	145.9	121.6	176.9	82.7	214.7
Ni₃Al_{0.625}Ge_{0.375}	3.574	5.0029	243.8	161.3	117	188.8	77.1	203.5
Ni₃Al_{0.5}Ge_{0.5}	3.5761	5.0096	248.2	153	114.8	184.73	80.6	211.2
Ni₃Al_{0.375}Ge_{0.625}	3.5767	5.0159	251.5	142.3	112.8	178.7	84.3	218.5
Ni₃Al_{0.25}Ge_{0.75}	3.5783	5.0223	251.1	136.8	110.6	174.9	84.9	219.1
Ni₃Al_{0.125}Ge_{0.875}	3.58	5.0294	264.9	147.7	108.2	186.6	84.7	220.6
Ni₃Ge	3.5805	5.0345	268.5	146.5	104.7	187.1	84.3	220

3.2 Bulk properties of Ni₃Si

Table 3 presents the bulk properties of Ni₃Si, where the calculated properties are compared with corresponding experimental values for comparison.

Table 3: Bulk properties for Ni₃Si and its comparison with experimental values

Ni ₃ Si	Calculated	Experimental [12]	Error (%)
Lattice parameter (Å)	3.5086	3.5096	0.03
Cohesive energy(eV/atom)	5.4239	5.7167	5.4
C₁₁ (Gpa)	305.1	270	13
C₁₂ (Gpa)	157.1	170	8.2
C₄₄ (Gpa)	129.1	125	3.3
Bulk modulus (Gpa)	206.4	201.7	2.3
Shear modulus (Gpa)	103.3	96.4	7.2
Young's modulus (Gpa)	265.5	249.45	6.4

3.2.1 Effect of Si on bulk properties of Ni₃Al_(1-x)Si_x

- Table 4 and Figure 5 provide the calculated bulk properties for different compositions of Ni₃Al_(1-x)Si_x. The data indicates that as the Si content increases progressively in the Ni₃Al alloy, two trends are observed: a decrease in the lattice parameter and an increase in cohesive energies.
- In the context of Ni₃Al_(1-x)Si_x compositions, the observed decrease in the lattice parameter as Si content increases implies that the incorporation of Si atoms into the Ni₃Al crystal structure results in a reduction in the distance between lattice points. This suggests a contraction or compression of the crystal lattice.
- On the other hand, the increase in cohesive energies with the progressive addition of Si in the Ni₃Al alloy indicates that the bonding between atoms becomes stronger and more stable. This suggests that the presence of Si enhances the cohesive forces within the material, leading to a higher energy requirement for atom separation.
- Taken together, it highlights that increasing Si content in the Ni₃Al alloy has two effects on the bulk properties. Firstly, it leads to a decrease in the lattice parameter, indicating a contraction of the crystal lattice. Secondly, it results in increased cohesive energies, reflecting stronger and more stable bonding between atoms.

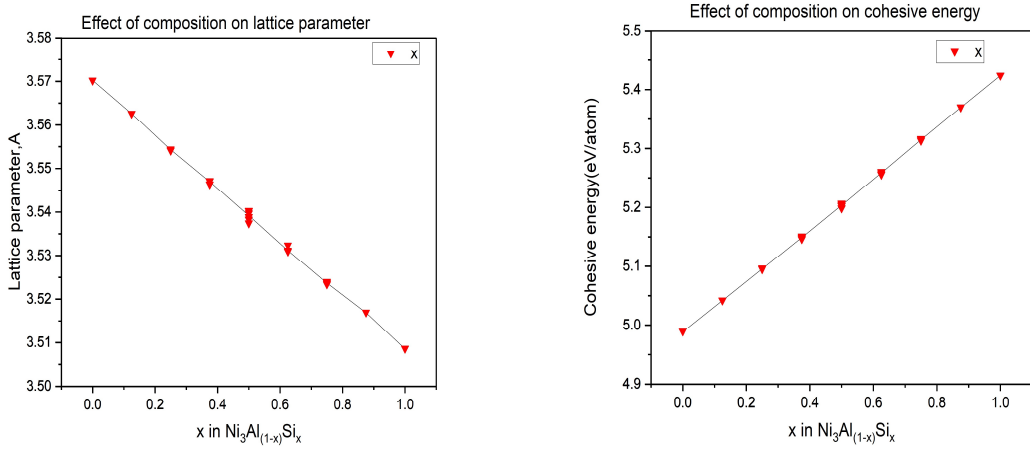


Figure 5: Effect of increase in Si content on bulk properties of $\text{Ni}_3\text{Al}_{(1-x)}\text{Si}_x$

3.2.2 Effect of Si on elastic constants of $\text{Ni}_3\text{Al}_{(1-x)}\text{Si}_x$

- Table 4 and Figure 6 present the calculated elastic constants for different compositions of $\text{Ni}_3\text{Al}_{(1-x)}\text{Si}_x$. It is observed that the progressive increase of Si content in the $\text{Ni}_3\text{Al}_{(1-x)}\text{Si}_x$ alloy system leads to different trends for the elastic constants C_{11} , C_{12} , and C_{44} , as depicted in Figure 6. Specifically, C_{11} increases with increasing Si content, while C_{12} remains relatively constant, and C_{44} initially decreases and then increases as Si content in Ni_3Al increases.
- The increase in C_{11} as Si content increases suggests that the material becomes stiffer along a specific crystallographic direction. This indicates that incorporating Si into the Ni_3Al alloy leads to enhanced resistance to deformation in that particular direction.
- On the other hand, the relatively constant values of C_{12} with increasing Si content indicate that the stiffness between different crystallographic planes does not vary significantly. This suggests that the addition of Si does not strongly influence the material's response to deformation across these planes.
- The trend observed for C_{44} , where it initially decreases and then increases with increasing Si content, indicates a more complex behaviour. The initial decrease in C_{44} suggests that the material becomes less resistant to shear deformation along a specific plane. However, as the Si content increases further, C_{44} starts to rise again, indicating a subsequent increase in the material's resistance to shear deformation.
- In summary, the sentence highlights that increasing Si content in the $\text{Ni}_3\text{Al}_{(1-x)}\text{Si}_x$ alloy has different effects on the elastic constants. C_{11} increases, indicating increased stiffness along a specific crystallographic direction. C_{12} remains relatively constant, indicating consistent stiffness between different planes. C_{44} initially decreases, implying reduced resistance to shear deformation, but then increases again, suggesting an eventual increase in resistance.

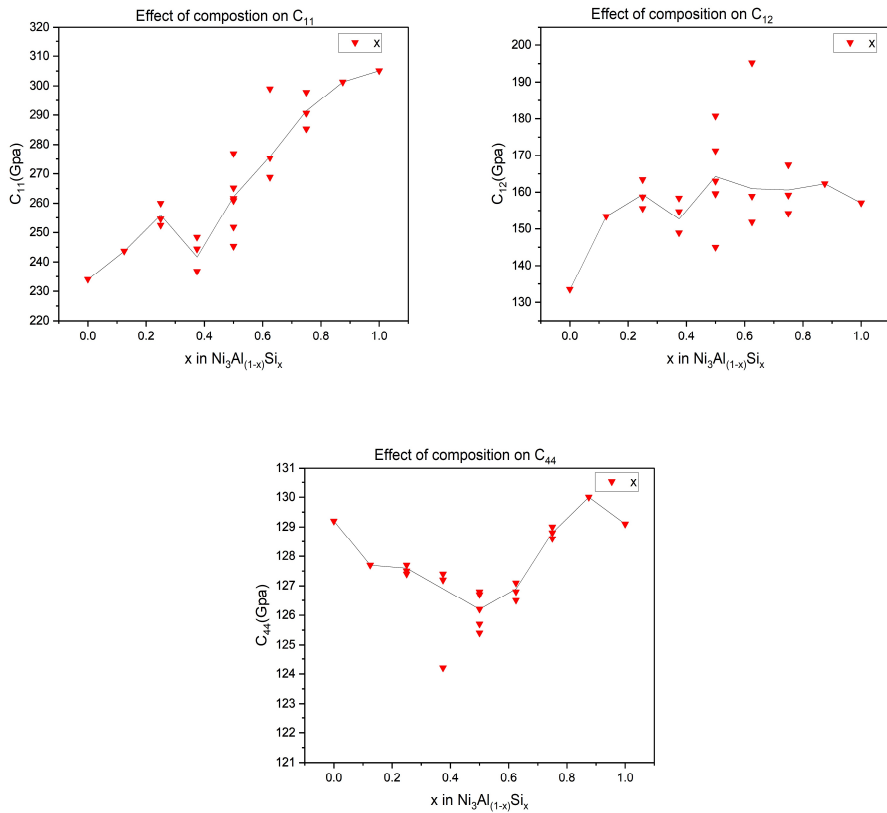


Figure 6: Effect of increase in Si content on elastic constants (C_{11} , C_{12} , C_{44}) of $\text{Ni}_3\text{Al}_{(1-x)}\text{Si}_x$

3.2.3 Effect of Si on mechanical properties (Bulk, Shear and Young's modulus) of $\text{Ni}_3\text{Al}_{(1-x)}\text{Si}_x$

- Table 4 and Figure 7 present the calculated mechanical properties, obtained using the Hill averaging method from elastic constants, for various compositions of $\text{Ni}_3\text{Al}_{(1-x)}\text{Si}_x$. The progressive increase of Si in the $\text{Ni}_3\text{Al}_{(1-x)}\text{Si}_x$ alloy system exhibits different trends for the bulk modulus, shear modulus, and Young's modulus, as depicted in Figure 7. Specifically, the bulk modulus generally increases with increasing Si content in Ni_3Al , but at a specific composition, it decreases. On the other hand, the shear modulus shows a general increasing trend with Si content, except for two points near lower Si content where it deviates from the increasing trend and decreases. The Young's modulus behaves similarly to the shear modulus.
- The mechanical properties of a material, such as the bulk modulus, shear modulus, and Young's modulus, provide insights into its response to different types of stress and deformation.

- In the case of $\text{Ni}_3\text{Al}_{(1-x)}\text{Si}_x$ compositions, the bulk modulus generally increases as the Si content in Ni_3Al increases. This suggests that the material becomes stiffer and more resistant to volume change under pressure. However, there is a specific composition where the bulk modulus decreases. This suggests that there may be a critical point or a change in the material's behaviour at that particular Si content.
- The shear modulus, which characterizes the material's resistance to deformation along planes parallel to the applied force, exhibits a general increasing trend with increasing Si content in Ni_3Al . This indicates that the material becomes stiffer in terms of shear resistance. However, at two points near lower Si content, there is a deviation from the increasing trend, and the shear modulus decreases. This suggests that there may be specific Si compositions where the material's response to shear deformation changes.
- Young's modulus, which represents the material's stiffness or resistance to elastic deformation under tension or compression, behaves similarly to the shear modulus. It follows a general increasing trend with increasing Si content in Ni_3Al , implying increased stiffness. The similarity in the trends of Young's modulus and shear modulus suggests a correlation between these two mechanical properties.
- Overall, the sentence highlights that the progressive increase of Si content in the $\text{Ni}_3\text{Al}_{(1-x)}\text{Si}_x$ alloy system results in different trends for the bulk modulus, shear modulus, and Young's modulus. The bulk modulus generally increases but decreases at a specific composition. The shear modulus shows an increasing trend but deviates and decreases at two points near lower Si content. The Young's modulus follows a similar trend to the shear modulus.

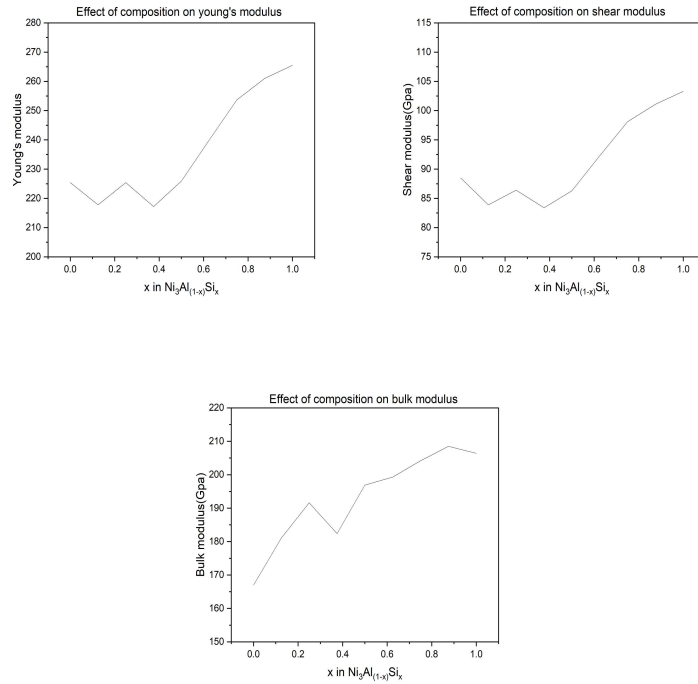


Figure 7: Effect of increase in Si content on mechanical properties (Bulk, Shear, Young's modulus) of $\text{Ni}_3\text{Al}_{(1-x)}\text{Si}_x$

3.2.4 Effect of Si on anisotropy ratio of $\text{Ni}_3\text{Al}_{(1-x)}\text{Si}_x$

- Figure 8 presents the calculated anisotropy ratio for different compositions of $\text{Ni}_3\text{Al}_{(1-x)}\text{Si}_x$. The progressive increase of Si in the Ni_3Al alloy is found to generally decrease the anisotropy ratio. However, at two compositions with lower Si content, there is an increase in the anisotropy ratio, deviating from the overall trend. Additionally, at very low Si additions, there is an initial increase in the anisotropy ratio.
- The anisotropy ratio represents the degree of variation in properties or behaviour of a material along different crystallographic directions. In the context of $\text{Ni}_3\text{Al}_{(1-x)}\text{Si}_x$ compositions, the anisotropy ratio provides insights into how the material's properties vary with Si content.
- The above statement highlights that as the Si content increases in the Ni_3Al alloy, the anisotropy ratio generally decreases. This suggests that the material becomes more isotropic, meaning its properties become more uniform or less dependent on the direction of measurement. The decrease in anisotropy ratio indicates a reduction in the variation of properties along different crystallographic directions.
- However, at two compositions with lower Si content, the anisotropy ratio increases. This implies that the material's properties exhibit more significant variations along different directions at these specific compositions, deviating from the overall trend.
- Additionally, it tells that at very low Si additions, there is an initial increase in the anisotropy ratio. This indicates that the material's properties initially show more pronounced variations along different directions with minimal Si content. However, as the Si content increases further, the anisotropy ratio decreases, suggesting a reduction in the variations and a trend toward isotropy.
- In summary, it conveys that the progressive increase of Si content in the Ni_3Al alloy leads to a decrease in the anisotropy ratio, indicating a trend towards isotropy. However, at two compositions with lower Si content, there is an increase in the anisotropy ratio, deviating from the general trend. Moreover, at very low Si additions, there is an initial increase in the anisotropy ratio before it starts to decrease.

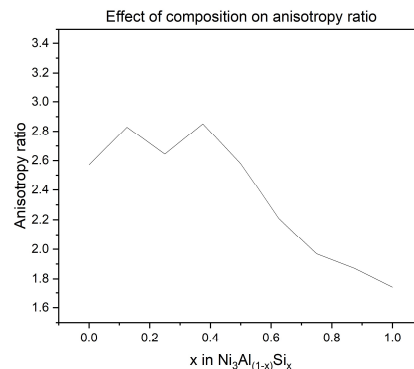


Figure 8: Effect of increase in Si content on anisotropy ratio of $\text{Ni}_3\text{Al}_{(1-x)}\text{Si}_x$

Table 4: Calculated bulk properties and elastic constants for different compositions of $Ni_3Al_{(1-x)}Si_x$

	Lattice parameter (Å)	Cohesive energy (eV/atom)	C_{11} (Gpa)	C_{12} (Gpa)	C_{44} (Gpa)	Bulk Modulus (Gpa)	Shear Modulus (Gpa)	Young's Modulus (Gpa)
Ni_3Al	3.5702	4.9891	234	133.5	129.2	167	88.5	225.4
$Ni_3Al_{0.875}Si_{0.125}$	3.5626	5.0422	243.7	153.4	127.7	181.1	83.9	217.8
$Ni_3Al_{0.75}Si_{0.25}$	3.5543	5.0956	255.9	159.4	127.6	191.6	86.4	225.4
$Ni_3Al_{0.625}Si_{0.375}$	3.547	5.1492	241.7	152.7	126.9	182.4	83.4	217.2
$Ni_3Al_{0.5}Si_{0.5}$	3.5392	5.2034	262.2	164.3	126.2	196.9	86.3	225.9
$Ni_3Al_{0.375}Si_{0.625}$	3.5312	5.2588	275.9	161	126.9	199.3	92.3	239.9
$Ni_3Al_{0.25}Si_{0.75}$	3.5237	5.3147	291.4	160.6	128.8	204.2	98.1	253.7
$Ni_3Al_{0.125}Si_{0.875}$	3.5169	5.37	301.3	162.3	130	208.5	101.1	261
Ni_3Si	3.5086	5.4239	305.1	157.1	129.1	206.4	103.3	265.5

3.3 Bulk properties of Ni_3Ge

Table 5 presents the bulk properties of Ni_3Ge , where the calculated properties are compared with corresponding experimental values for comparison.

Table 5: Bulk properties for Ni_3Ge and its comparison with experimental values

Ni_3Ge	Calculated	Experimental [14]	Error (%)
Lattice parameter (Å)	3.5805	3.579	0.04
Cohesive energy (eV/atom)	5.0345	5.3567	6.4
C_{11} (Gpa)	268.5	253	6.1
C_{12} (Gpa)	146.5	135	8.5
C_{44} (Gpa)	104.7	107	2.2
Bulk modulus (Gpa)	187.1	175	6.9
Shear modulus (Gpa)	84.3	84	0.35
Young's modulus (Gpa)	220	217.2	1.3

3.3.1 Effect of Si on bulk properties of $Ni_3Ge_{(1-x)}Si_x$

- Table 6 and Figure 9 provide the calculated bulk properties for different compositions of $Ni_3Ge_{(1-x)}Si_x$. The data indicates that as the Si content increases progressively in the Ni_3Ge alloy, two trends are observed: a decrease in the lattice parameter and an increase in cohesive energies.
- In the context of $Ni_3Ge_{(1-x)}Si_x$ compositions, the observed decrease in the lattice parameter and increase in cohesive energies with increasing Si content provide valuable insights into the structural and energetic characteristics of the alloy system.
- The decrease in the lattice parameter as Si content increases suggests a contraction or compression of the crystal lattice. Incorporating Si atoms into the Ni_3Ge alloy leads to

a reduction in the distance between lattice points, resulting in a smaller lattice parameter. This indicates that the presence of Si induces structural changes and modifies the arrangement of atoms within the crystal lattice.

- Simultaneously, the increase in cohesive energies with the progressive addition of Si implies stronger and more stable bonding between atoms in the $\text{Ni}_3\text{Ge}_{(1-x)}\text{Si}_x$ compositions. The addition of Si enhances the cohesive forces within the material, leading to a higher energy requirement for atom separation. This increase in cohesive energies indicates a greater degree of atomic bonding and stability in the alloy system.
- Overall, it conveys that increasing Si content in the Ni_3Ge alloy has two effects on the bulk properties. Firstly, it leads to a decrease in the lattice parameter, indicating a compression of the crystal lattice. Secondly, it results in increased cohesive energies, reflecting stronger and more stable bonding between atoms.

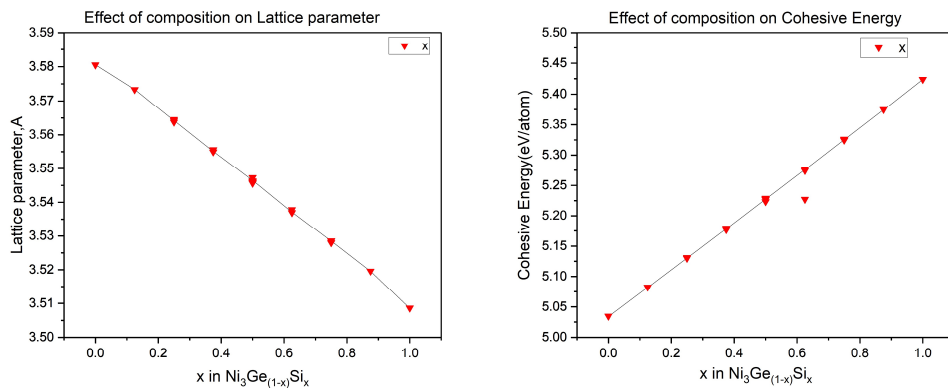


Figure 9: Effect of increase in Si content on bulk properties of $\text{Ni}_3\text{Ge}_{(1-x)}\text{Si}_x$

3.3.2 Effect of Si on elastic constants of $\text{Ni}_3\text{Ge}_{(1-x)}\text{Si}_x$

- Table 6 and Figure 10 display the calculated elastic constants for different compositions of $\text{Ni}_3\text{Ge}_{(1-x)}\text{Si}_x$. The results demonstrate that the progressive increase of Si content in the $\text{Ni}_3\text{Ge}_{(1-x)}\text{Si}_x$ alloy system exhibits distinct trends for the elastic constants C_{11} , C_{12} , and C_{44} , as depicted in Figure 10. Specifically, both C_{11} and C_{12} increase as Si content increases, with two notable peaks observed around intermediate compositions. In contrast, C_{44} shows a linear increase with increasing Si content.
- In the context of $\text{Ni}_3\text{Ge}_{(1-x)}\text{Si}_x$ compositions, the observed trends for C_{11} , C_{12} , and C_{44} shed light on the anisotropy and mechanical properties of the alloy system.
- It highlights that both C_{11} and C_{12} increase as Si content in the $\text{Ni}_3\text{Ge}_{(1-x)}\text{Si}_x$ alloy compositions increases. This indicates that the material becomes stiffer and exhibits enhanced resistance to deformation along specific crystallographic directions and also between specific crystallographic planes. Moreover, two notable peaks are observed around intermediate compositions, suggesting that there are specific Si content values where the stiffness of the material is significantly higher.
- On the other hand, C_{44} shows a linear increase with increasing Si content. C_{44} represents the resistance to shear deformation in a specific crystallographic plane. The observed

linear increase implies that as Si content increases, the material becomes progressively more resistant to shear deformation along this particular plane.

- The distinct trends observed for C_{11} , C_{12} , and C_{44} emphasize the anisotropic nature of the $\text{Ni}_3\text{Ge}_{(1-x)}\text{Si}_x$ alloy system. Anisotropy refers to the variation in mechanical properties or behaviour of a material along different crystallographic directions. The increasing values of C_{11} and C_{12} with Si content indicate a strengthening of the material in specific directions, while the linear increase in C_{44} reflects enhanced resistance to shear deformation along a particular plane.

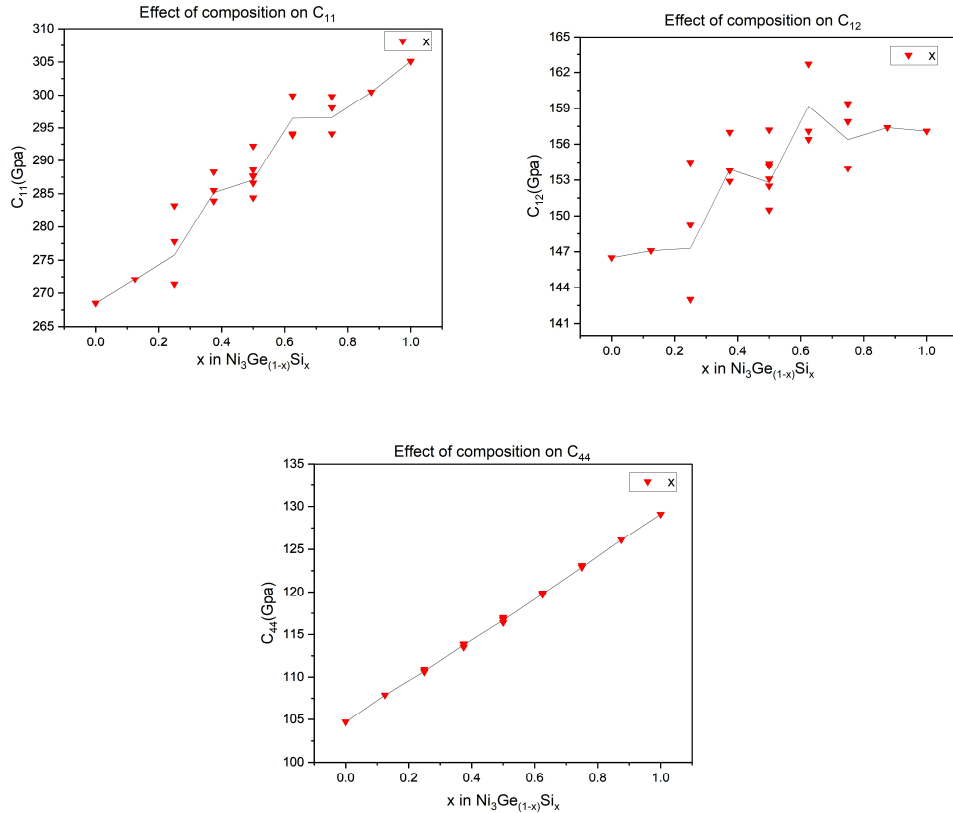


Figure 10: Effect of increase in Si content on elastic constants (C_{11} , C_{12} , C_{44}) of $\text{Ni}_3\text{Ge}_{(1-x)}\text{Si}_x$

3.3.3 Effect of Si on mechanical properties (Bulk, Shear and Young's modulus) of $\text{Ni}_3\text{Ge}_{(1-x)}\text{Si}_x$

- Table 6 and Figure 11 present the calculated mechanical properties, obtained using the Hill averaging method from elastic constants, for different compositions of $\text{Ni}_3\text{Ge}_{(1-x)}\text{Si}_x$. The results indicate that the progressive increase of Si content in the $\text{Ni}_3\text{Ge}_{(1-x)}\text{Si}_x$ alloy system leads to distinct increasing trends in the Bulk, Shear, and Young's modulus, as illustrated in Figure 11. Specifically, both the Shear and Young's modulus of $\text{Ni}_3\text{Ge}_{(1-x)}\text{Si}_x$ compositions demonstrate a linear trend upon the addition of Si, while

the Bulk modulus increases with increasing Si content, showing two notable peaks in the linear trend around intermediate compositions.

- Both Shear and Young's modulus of $\text{Ni}_3\text{Ge}_{(1-x)}\text{Si}_x$ compositions show a linear increasing trend with the addition of Si. This suggests that the material becomes stiffer and exhibits enhanced resistance to deformation as Si content increases. The linear increase indicates a proportional relationship between the Si content and the values of Shear and Young's modulus. This behaviour implies that the addition of Si effectively contributes to the strengthening of the material in terms of its ability to resist shear and overall deformation.
- Furthermore, the Bulk modulus demonstrates an increasing trend with increasing Si content. The Bulk modulus represents the material's resistance to uniform compression or volumetric deformation. The observed increase indicates that as Si content increases, the material becomes less compressible and more resistant to uniform deformation. Notably, two prominent peaks are observed in the linear trend around intermediate compositions. These peaks indicate specific Si content values where the material exhibits even higher resistance to compression.
- Interpreting the trends, it is evident that the progressive addition of Si in the $\text{Ni}_3\text{Ge}_{(1-x)}\text{Si}_x$ alloy system enhances its mechanical properties. Both Shear and Young's modulus exhibit a linear increase, indicating a consistent improvement in the material's stiffness and resistance to deformation. The increasing Bulk modulus signifies a greater resistance to volumetric deformation, with notable enhancements at intermediate compositions.

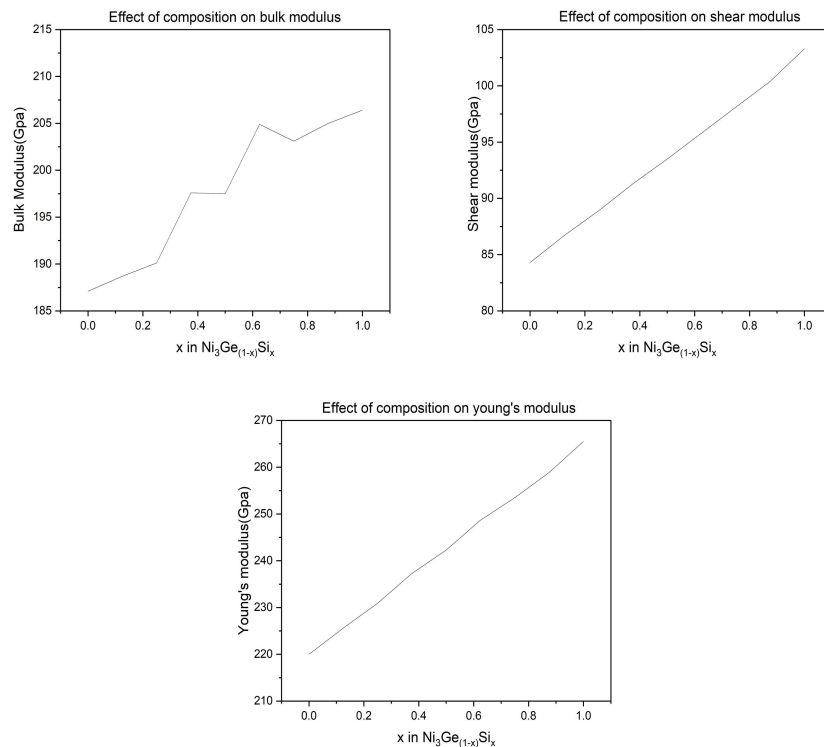


Figure 11: Effect of increase in Si content on mechanical properties (Bulk, Shear, Young's modulus) of $\text{Ni}_3\text{Ge}_{(1-x)}\text{Si}_x$

3.3.4 Effect of Si on anisotropy ratio of $\text{Ni}_3\text{Ge}_{(1-x)}\text{Si}_x$

- Figure 12 illustrates the calculated anisotropy ratio for different compositions of $\text{Ni}_3\text{Ge}_{(1-x)}\text{Si}_x$. The results indicate that as the Si content progressively increases in the Ni_3Ge alloy, the anisotropy ratio also increases. However, there are deviations from this trend at lower Si content, where the anisotropy ratio decreases, and at higher Si content, where it increases slightly than observed trend.
- The anisotropy ratio is a measure of the difference in physical properties along different crystallographic directions in a material. In the context of $\text{Ni}_3\text{Ge}_{(1-x)}\text{Si}_x$ compositions, the anisotropy ratio provides insights into the directional dependence of the material's properties and behaviour.
- The anisotropy ratio increases with the progressive increase of Si content in the $\text{Ni}_3\text{Ge}_{(1-x)}\text{Si}_x$ alloy compositions. This suggests that the material becomes more anisotropic as more Si is added. The increase in the anisotropy ratio indicates a greater variation in the material's properties and behaviour along different crystallographic directions.
- However, there are deviations from this increasing trend at lower and higher Si content. At lower Si content, the anisotropy ratio decreases, implying a reduced variation in properties along different directions. This deviation suggests that the addition of a small amount of Si influences the material's anisotropy in a different manner. Similarly, at higher Si content, the anisotropy ratio increases, indicating an enhanced variation in properties along different crystallographic directions. This deviation suggests that the influence of a higher Si content on the material's anisotropy differs from the progressive trend observed at intermediate compositions.
- Interpreting the trends, indicates that the progressive addition of Si in the Ni_3Ge alloy increases the anisotropy ratio, signifying a greater difference in properties along different crystallographic directions. However, the deviations observed at lower and higher Si content indicate that the effect of Si on the anisotropy ratio is not solely dependent on its quantity. Other factors such as atomic arrangement, crystal structure, and interactions between Si and other elements in the alloy may contribute to these deviations.

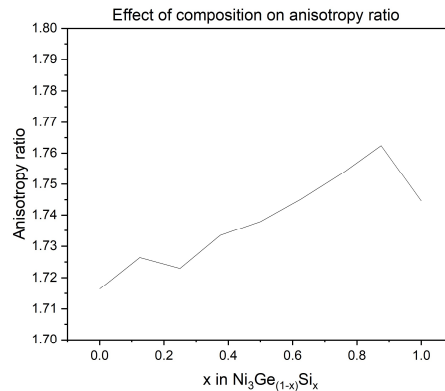


Figure 12: Effect of increase in Si content on anisotropy ratio of $\text{Ni}_3\text{Ge}_{(1-x)}\text{Si}_x$

Table 6: Calculated bulk properties and elastic constants for different compositions of $Ni_3Ge-(1-x)Si_x$

	Lattice parameter (Å)	Cohesive energy (eV/atom)	C_{11} (Gpa)	C_{12} (Gpa)	C_{44} (Gpa)	Bulk Modulus (Gpa)	Shear Modulus (Gpa)	Young's Modulus (Gpa)
Ni_3Ge	3.5805	5.0345	268.5	146.5	104.7	187.1	84.3	220
$Ni_3Ge_{0.875}Si_{0.125}$	3.5734	5.0823	272.1	147.1	107.9	188.7	86.7	225.6
$Ni_3Ge_{0.75}Si_{0.25}$	3.5642	5.1304	275.8	147.3	110.7	190.1	88.9	230.9
$Ni_3Ge_{0.625}Si_{0.375}$	3.5551	5.1787	285.2	153.9	113.8	197.6	91.3	237.3
$Ni_3Ge_{0.5}Si_{0.5}$	3.5465	5.2273	287.1	152.8	116.7	197.5	93.5	242.3
$Ni_3Ge_{0.375}Si_{0.625}$	3.5371	5.2761	296.5	159.2	119.8	204.9	95.8	248.7
$Ni_3Ge_{0.25}Si_{0.75}$	3.5285	5.3252	296.6	156.4	122.9	203.1	98.1	253.5
$Ni_3Ge_{0.125}Si_{0.875}$	3.5196	5.3747	300.5	157.4	126.1	205	100.4	258.9
Ni_3Si	3.5086	5.4239	305.1	157.1	129.1	206.4	103.3	265.5

Chapter 4

Descriptors of the configurations

4.1 Feature selection

The radial distribution function (RDF) is a commonly used descriptor in the field of materials science and molecular dynamics simulations. It provides information about the distribution of particles or atoms in a system as a function of their distance from a reference particle.

When using RDF as a descriptor, several characteristics or features can be extracted from the RDF curve to describe the configurations of the system. Here are some common descriptors derived from the RDF.

1. Peak positions: The positions of the prominent peaks in the RDF curve correspond to the average distances between atoms or particles in the system. These positions can provide information about the coordination number and bonding distances.
2. Peak heights: The heights of the peaks in the RDF curve represent the relative abundance of atoms or particles at specific distances. Higher peak heights indicate stronger correlations or higher densities of atoms at those distances.
3. Coordination numbers: The areas under the peaks in the RDF curve are related to the coordination numbers, which indicate the average number of neighbouring particles within a certain distance from a reference particle. The integration of peak areas can provide insights into the local structure of the system.
4. Bond lengths: The distances corresponding to the peaks in the RDF curve can be associated with specific types of bonds in the system. By analysing these distances, one can identify characteristic bond lengths and infer the types of chemical bonds present.
5. Structure ordering: The overall shape and fluctuations of the RDF curve can reveal the level of order or disorder in the system. Well-defined peaks and a smooth curve suggest a more ordered structure, while broad or irregular features indicate a more disordered or amorphous arrangement.
6. Long-range order: In addition to local structure information, the RDF can provide insights into the long-range ordering of particles in the system. By examining the decay of the RDF curve at large distances, one can infer the presence of periodic or quasi-periodic arrangements.
 - One of these descriptors of above-mentioned used to study the bonding characteristics in materials is the coordination number. In the context of the alloys $\text{Ni}_3\text{Al}_{(1-x)}\text{Ge}_x$, $\text{Ni}_3\text{Ge}_{(1-x)}\text{Si}_x$ and $\text{Ni}_3\text{Si}_{(1-x)}\text{Ge}_x$, the coordination number can provide information about the number of nearest neighbouring atoms or particles of a specific type.

- The configuration descriptors are obtained from the unrelaxed structures by importing them as XYZ files from Vienna Ab initio Simulation Package (VASP). These structures are visualized using Ovito software. Once the radial distribution values are generated from the software, they are employed to calculate the number of nearest neighbour atoms (up to the third nearest neighbour) in the lattices of (Al, Ge), (Si, Ge), and (Si, Al) sites within the $\text{Ni}_3\text{Al}_{(1-x)}\text{Ge}_x$, $\text{Ni}_3\text{Ge}_{(1-x)}\text{Si}_x$ and $\text{Ni}_3\text{Si}_{(1-x)}\text{Ge}_x$ alloys, respectively using the formula as follows.
- To determine the coordination numbers for different bond types, we had employed the following formula:

$$N_{x-x} = G(r) * 4\pi R^2 dr * C_x^2 / a^3 \quad (28)$$

$$N_{y-y} = G(r) * 4\pi R^2 dr * C_y^2 / a^3 \quad (29)$$

$$N_{x-y} = G(r) * 4\pi R^2 dr * 2C_x C_y / a^3 \quad (30)$$

Where,

$G(r)$ = radial distribution value = (local density / total density) of atom

dr = histogram bin size

a = lattice parameter

C_x = weighted fraction of x

C_y = weighted fraction of y

R = radius

N_{x-x} , N_{x-y} , N_{y-y} are the number of nearest neighbors of $x-x$, $x-y$, $y-y$ types.

Both x , y represents {Aluminium (Al), Silicon (Si) and Germanium (Ge)}

Example of the representation of descriptors of a configuration is shown in the figure below.

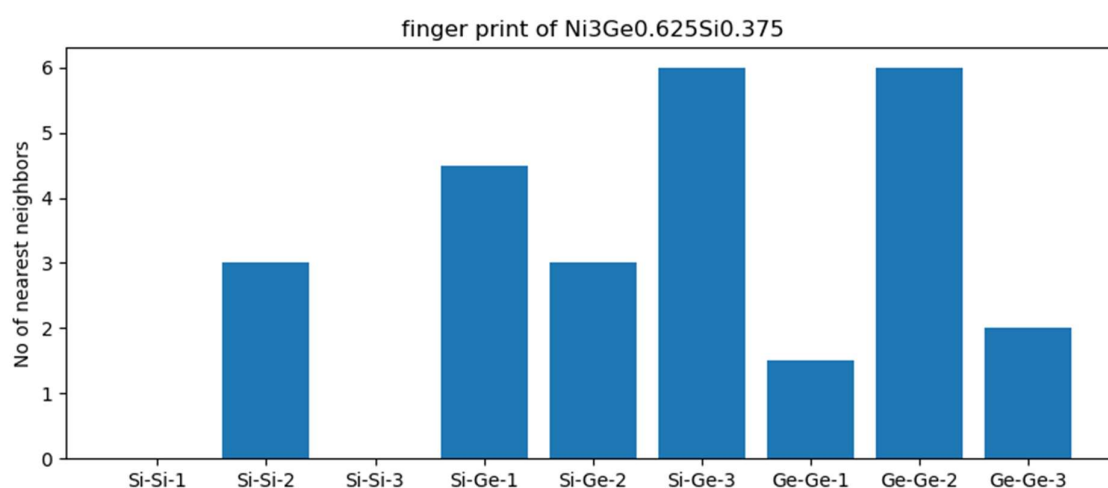


Figure 13: Bar plot represents the number of 1st, 2nd, 3rd nearest neighbour bonds of type Si-Si, Si-Ge, Ge-Ge in $\text{Ni}_3\text{Ge}_{0.25}\text{Si}_{0.375}$ configuration.

- In order to predict the properties of the ternary pseudo-binary alloy $\text{Ni}_3\text{Al}_{(1-x-y)}\text{Ge}_x\text{Si}_y$ using machine learning (ML) models, calculations of radial distribution function (RDF) were performed for all the configurations of the compositions of the alloys $\text{Ni}_3\text{Al}_{(1-x)}\text{Ge}_x$, $\text{Ni}_3\text{Ge}_{(1-x)}\text{Si}_x$ and $\text{Ni}_3\text{Si}_{(1-x)}\text{Ge}_x$, where x varies from 0 to 1. As the RDF calculations provides information about the 1st, 2nd, and 3rd nearest neighbours of various bond types, including Al-Al, Al-Si, Si-Si, Si-Ge, and Ge-Ge, Al-Ge.
- The data obtained for the 1st, 2nd, and 3rd nearest neighbour bonds of the aforementioned bond types of the respective configurations of $\text{Ni}_3\text{Al}_{(1-x)}\text{Ge}_x$, $\text{Ni}_3\text{Ge}_{(1-x)}\text{Si}_x$ and $\text{Ni}_3\text{Si}_{(1-x)}\text{Ge}_x$ systems, were used as features for training machine learning models such as Random forest regression, Support vector machine(SVM) regression, and XGboost. The corresponding properties of the systems, such as 9 elastic constants which are averaged to three(Kim et al., 2010; Wu & Li, 2012a)[16-17] ,were used as the output for these ML models.

4.2 ML model selection

- The selection of a machine learning algorithm is a crucial step in building a statistical model, just like the feature selection process. The choice of algorithm depends on the number of outputs required for the dataset. Initially, for the three averaged elastic constants (C_{11} , C_{12} , C_{44}), support vector machine (SVM), random forest, and XGBoost were found to be suitable when training the models independently. However, when attempting to perform regression between 18 input features and 9 elastic constants, using scikit-learn-based algorithms becomes impractical. SVM does not support multiple output regression, while random forest and XGBoost do support it. Nevertheless, these algorithms require larger datasets for training, as they divide the data into multiple subsets for each tree and generate hyperparameters based on validation scores. Since the available datasets are small, this approach is not feasible. To overcome this limitation, neural network (NN)-based machine learning algorithms are employed in this study for multiple regression problems. The hyperas optimization technique is used to optimize various hyperparameters, such as the optimizer, number of neurons, activation function, layers, batch size, regularization strength (L1, L2), and epochs. Along with K-fold cross-validation, in the neural network model, the Huber loss function was implemented to evaluate the loss. This loss function is a robust fit function that lies between the mean absolute error (MAE) and the root mean squared error (RMSE). Its implementation was specifically chosen considering the small size of the dataset, aiming to improve the model's performance and stability.

4.3 ML-NN model training and testing

- To develop a robust machine learning model, it is essential to have data for training, validation, and testing purposes. In this study, two different splits of data percentages were utilized: 75:25 and 50:50. Randomly selected 75% and 50% of the respective splits were used to train two different models, while the remaining percentages of data were reserved for testing the final model's performance on unseen data. Due to the small size of the datasets, the K-fold cross-validation technique was employed. The validation data percentage was determined based on the number of folds used for cross-validation, which was set equal to the input shape of the training dataset. Each data sample was cross validated to identify the optimal hyperparameters for the model. Notably, increasing the amount of data fed into the model resulted in improved accuracy on the testing dataset. To assess the influence of training dataset size on the model's predictive performance on unseen. Furthermore, two metrics, namely mean absolute error (MAE) and coefficient of determination (r^2), were consistently employed to quantify the predictive performance of the model during the model building, testing, and prediction stages. MAE is a commonly used metric that provides a measure of closeness to the true values, while r^2 is a standard measure of goodness of fit, indicating the proportion of variation in the dependent variable that can be predicted from the independent variable. As the study focuses on three different alloy systems: $\text{Ni}_3\text{Al}_{(1-x)}\text{Ge}_x$, $\text{Ni}_3\text{Ge}_{(1-x)}\text{Si}_x$ and $\text{Ni}_3\text{Si}_{(1-x)}\text{Ge}_x$, comprising a total of 63 configurations. The training and testing datasets mentioned earlier consist of an equal amount of data from all three alloy systems.

Chapter 5

Results and discussions of ML-NN predicted data

Table 7: First nearest neighbours up to 3 of bond types of Al-Al, Si-Al, Si-Si, Ge-Al, Si-Ge, Ge-Ge in $Ni_3Al_{(1-x)}Ge_x$ compositions and it's different configurations.

Bond type Al-Al	Bond type														
	Si-Al			Si-Si			Ge-Al			Si-Ge			Ge-Ge		
	Nearest neighbour bonds			Nearest neighbour bonds			Nearest neighbour bonds			Nearest neighbour bonds			Nearest neighbour bonds		
$Ni_3Al_{(1-x)}Ge_x$	1st	2nd	3rd												
Ni_3Al	6	12	8	0	0	0	0	0	0	0	0	0	0	0	0
$Ni_3Al_{0.875}Ge_{0.125}$	4.5	9	6	0	0	0	0	0	0	0	0	0	0	0	0
$Ni_3Al_{0.75}Ge_{0.25}$	3	6	6	0	0	0	0	0	0	3	6	0	0	0	2
$Ni_3Al_{0.625}Ge_{0.375}$ -1	3.5	6	4	0	0	0	0	0	0	2	6	4	0	0	0
$Ni_3Al_{0.625}Ge_{0.375}$ -2	3	7	4	0	0	0	0	0	0	3	4	4	0	0	0
$Ni_3Al_{0.625}Ge_{0.375}$ -3	1.5	6	2	0	0	0	0	0	0	4.5	3	6	0	0	0
$Ni_3Al_{0.625}Ge_{0.375}$ -4	2	4	4	0	0	0	0	0	0	3.5	7	2	0	0	0
$Ni_3Al_{0.625}Ge_{0.375}$ -5	2.5	4	2	0	0	0	0	0	0	2.5	7	6	0	0	0
$Ni_3Al_{0.5}Ge_{0.5}$	0	6	0	0	0	0	0	0	0	6	0	8	0	0	0
$Ni_3Al_{0.5}Ge_{0.5}$ -1	1	2	4	0	0	0	0	0	0	4	8	0	0	0	4
$Ni_3Al_{0.5}Ge_{0.5}$ -2	2	2	0	0	0	0	0	0	0	2	8	8	0	0	0
$Ni_3Al_{0.5}Ge_{0.5}$ -3	1.5	3	0	0	0	0	0	0	0	3	6	8	0	0	0
$Ni_3Al_{0.5}Ge_{0.5}$ -4	1.5	2	2	0	0	0	0	0	0	3	8	4	0	0	0
$Ni_3Al_{0.5}Ge_{0.5}$ -5	1	3	2	0	0	0	0	0	0	4	6	4	0	0	0
$Ni_3Al_{0.375}Ge_{0.625}$	0	3	0	0	0	0	0	0	0	4.5	3	6	0	0	0
$Ni_3Al_{0.375}Ge_{0.625}$ -1	0.5	1	2	0	0	0	0	0	0	3.5	7	2	0	0	0
$Ni_3Al_{0.375}Ge_{0.625}$ -2	1	1	0	0	0	0	0	0	0	2.5	7	6	0	0	0
$Ni_3Al_{0.25}Ge_{0.75}$	0	0	0	0	0	0	0	0	0	3	6	0	0	0	6
$Ni_3Al_{0.25}Ge_{0.75}$ -1	0.5	0	0	0	0	0	0	0	0	2	6	4	0	0	0
$Ni_3Al_{0.25}Ge_{0.75}$ -2	0	1	0	0	0	0	0	0	0	3	4	4	0	0	0
$Ni_3Al_{0.125}Ge_{0.875}$	0	0	0	0	0	0	0	0	0	1.5	3	2	0	0	0

Table 8: Nine different DFT simulated elastic constants (in Gpa) for the compositions of $\text{Ni}_3\text{Al}_{(1-x)}\text{Ge}_x$

$\text{Ni}_3\text{Al}_{(1-x)}\text{Ge}_x$	C11	C22	C33	C12	C13	C23	C44	C55	C66
Ni_3Al	234	234	234	134	134	134	129	129	129
$\text{Ni}_3\text{Al}_{0.875}\text{Ge}_{0.125}$	240	240	241	154	154	154	123	121	121
$\text{Ni}_3\text{Al}_{0.75}\text{Ge}_{0.25}$	247	251	261	157	162	165	121	121	121
$\text{Ni}_3\text{Al}_{0.75}\text{Ge}_{0.25}-1$	234	234	235	153	155	155	118	118	118
$\text{Ni}_3\text{Al}_{0.75}\text{Ge}_{0.25}-2$	245	252	241	154	149	152	122	122	122
$\text{Ni}_3\text{Al}_{0.625}\text{Ge}_{0.375}$	235	234	239	151	154	153	117	117	117
$\text{Ni}_3\text{Al}_{0.625}\text{Ge}_{0.375}-1$	242	244	244	151	150	151	118	118	119
$\text{Ni}_3\text{Al}_{0.625}\text{Ge}_{0.375}-2$	235	234	234	157	157	157	116	116	116
$\text{Ni}_3\text{Al}_{0.5}\text{Ge}_{0.5}$	255	252	247	166	163	162	114	114	114
$\text{Ni}_3\text{Al}_{0.5}\text{Ge}_{0.5}-1$	238	244	256	149	158	157	115	116	116
$\text{Ni}_3\text{Al}_{0.5}\text{Ge}_{0.5}-2$	242	250	250	149	149	151	115	115	115
$\text{Ni}_3\text{Al}_{0.5}\text{Ge}_{0.5}-3$	249	246	249	155	156	155	114	114	114
$\text{Ni}_3\text{Al}_{0.5}\text{Ge}_{0.5}-4$	246	248	248	151	151	149	114	114	115
$\text{Ni}_3\text{Al}_{0.5}\text{Ge}_{0.5}-5$	240	248	248	146	146	150	114	115	115
$\text{Ni}_3\text{Al}_{0.375}\text{Ge}_{0.625}$	254	255	254	152	152	152	112	112	112
$\text{Ni}_3\text{Al}_{0.375}\text{Ge}_{0.625}-1$	257	254	255	148	148	149	112	112	113
$\text{Ni}_3\text{Al}_{0.375}\text{Ge}_{0.625}-2$	249	257	237	141	148	147	116	116	116
$\text{Ni}_3\text{Al}_{0.25}\text{Ge}_{0.75}$	262	265	261	149	146	148	111	111	111
$\text{Ni}_3\text{Al}_{0.25}\text{Ge}_{0.75}-1$	263	262	265	148	149	148	111	111	111
$\text{Ni}_3\text{Al}_{0.25}\text{Ge}_{0.75}-2$	269	263	263	151	151	147	111	111	111
$\text{Ni}_3\text{Al}_{0.125}\text{Ge}_{0.875}$	266	263	266	147	148	147	108	108	108

Table 9: First nearest neighbours up to 3 of bond types of Al-Al, Si-Al, Si-Si, Ge-Al, Si-Ge, Ge-Ge in $Ni_3Al_{(1-x)}Si_x$ compositions and it's different configurations

Bond type		Bond type			Bond type			Bond type			Bond type			Bond type			
Al-Al		Si-Al		Si-Si		Ge-Al		Si-Ge		Ge-Ge		Ge-Ge		Ge-Ge		Ge-Ge	
Nearest neighbour bond		Nearest neighbour bond			Nearest neighbour bond			Nearest neighbour bond			Nearest neighbour bond			Nearest neighbour bond			
$Ni_3Al_{(1-x)}Si_x$		1st	2nd	3rd	1st	2nd	3rd	1st	2nd	3rd	1st	2nd	3rd	1st	2nd	3rd	
Ni_3Si	0	0	0	0	0	0	0	6	12	8	0	0	0	0	0	0	0
$Ni_3Al_{0.875}Si_{0.125}$	4.5	9	6	1.5	3	2	0	0	0	0	0	0	0	0	0	0	0
$Ni_3Al_{0.75}Si_{0.25}$	3	6	6	3	6	0	0	2	0	0	0	0	0	0	0	0	0
$Ni_3Al_{0.75}Si_{0.25-1}$	3.5	6	4	2	6	4	0.5	0	0	0	0	0	0	0	0	0	0
$Ni_3Al_{0.75}Si_{0.25-2}$	3	7	4	3	4	4	0	1	0	0	0	0	0	0	0	0	0
$Ni_3Al_{0.625}Si_{0.375}$	1.5	6	2	4.5	3	6	0	3	0	0	0	0	0	0	0	0	0
$Ni_3Al_{0.625}Si_{0.375-1}$	2	4	4	3.5	7	2	0.5	1	2	0	0	0	0	0	0	0	0
$Ni_3Al_{0.625}Si_{0.375-2}$	2.5	4	2	2.5	7	6	1	1	0	0	0	0	0	0	0	0	0
$Ni_3Al_{0.625}Si_{0.375-2}$	0	6	0	6	0	8	0	6	0	0	0	0	0	0	0	0	0
$Ni_3Al_{0.5}Si_{0.5}$	1	2	4	4	8	0	1	2	4	0	0	0	0	0	0	0	0
$Ni_3Al_{0.5}Si_{0.5-2}$	2	2	0	2	8	8	2	2	0	0	0	0	0	0	0	0	0
$Ni_3Al_{0.5}Si_{0.5-3}$	1.5	3	0	3	6	8	1.5	3	0	0	0	0	0	0	0	0	0
$Ni_3Al_{0.5}Si_{0.5-4}$	1.5	2	2	3	8	4	1.5	2	2	0	0	0	0	0	0	0	0
$Ni_3Al_{0.5}Si_{0.5-5}$	1	3	2	4	6	4	1	3	2	0	0	0	0	0	0	0	0
$Ni_3Al_{0.375}Si_{0.625}$	0	3	0	4.5	3	6	1.5	6	2	0	0	0	0	0	0	0	0
$Ni_3Al_{0.375}Si_{0.625-1}$	0.5	1	2	3.5	7	2	4	4	0	0	0	0	0	0	0	0	0
$Ni_3Al_{0.375}Si_{0.625-2}$	1	1	0	2.5	7	6	2.5	4	2	0	0	0	0	0	0	0	0
$Ni_3Al_{0.25}Ge_{0.75}$	0	0	2	3	6	0	3	6	6	0	0	0	0	0	0	0	0
$Ni_3Al_{0.25}Ge_{0.75-1}$	0.5	0	0	2	6	4	3.5	6	4	0	0	0	0	0	0	0	0
$Ni_3Al_{0.25}Ge_{0.75-2}$	0	1	0	3	4	4	3	7	4	0	0	0	0	0	0	0	0
$Ni_3Al_{0.125}Si_{0.875}$	0	0	0	1.5	3	2	4.5	9	6	0	0	0	0	0	0	0	0

Table 10: Nine different DFT simulated elastic constants (in Gpa) for the compositions of $Ni_3Al_{(1-x)}Si_x$

$Ni_3Al_{(1-x)}Si_x$	C11	C22	C33	C12	C13	C23	C44	C55	C66
Ni_3Si	305	305	305	157	157	157	129	129	129
$Ni_3Al_{0.875}Si_{0.125}$	245	240	241	152	152	151	123	123	123
$Ni_3Al_{0.75}Si_{0.25}$	250	263	251	160	155	161	127	127	128
$Ni_3Al_{0.75}Si_{0.25}-1$	246	246	246	158	159	159	127	124	127
$Ni_3Al_{0.75}Si_{0.25}-2$	248	255	255	154	154	158	128	127	127
$Ni_3Al_{0.625}Si_{0.375}$	252	245	248	158	160	157	124	124	124
$Ni_3Al_{0.625}Si_{0.375}-1$	238	241	257	150	159	150	127	127	128
$Ni_3Al_{0.625}Si_{0.375}-2$	252	240	241	156	158	151	127	127	127
$Ni_3Al_{0.5}Si_{0.5}$	253	252	250	164	163	162	126	126	126
$Ni_3Al_{0.5}Si_{0.5}-1$	251	250	259	170	166	167	123	123	126
$Ni_3Al_{0.5}Si_{0.5}-2$	248	267	271	159	161	167	126	126	125
$Ni_3Al_{0.5}Si_{0.5}-3$	251	260	274	154	161	163	127	127	127
$Ni_3Al_{0.5}Si_{0.5}-4$	261	270	252	163	156	160	127	127	127
$Ni_3Al_{0.5}Si_{0.5}-5$	276	260	260	174	174	165	125	126	126
$Ni_3Al_{0.375}Si_{0.625}$	268	268	270	161	161	160	126	126	126
$Ni_3Al_{0.375}Si_{0.625}-1$	275	283	283	160	162	160	127	127	127
$Ni_3Al_{0.375}Si_{0.625}-2$	281	273	281	160	164	159	127	127	127
$Ni_3Al_{0.25}Ge_{0.75}$	290	293	290	160	158	160	129	129	129
$Ni_3Al_{0.25}Ge_{0.75}-1$	297	300	296	167	167	168	129	129	129
$Ni_3Al_{0.25}Ge_{0.75}-2$	272	289	295	150	152	161	129	129	129
$Ni_3Al_{0.125}Si_{0.875}$	302	306	296	165	160	162	130	130	130

Table 11: First nearest neighbours up to 3 of bond types of Al-Al, Si-Al, Si-Si, Ge-Al, Si-Ge, Ge-Ge in $Ni_3Ge_{(1-x)}Si_x$ compositions and it's different configurations.

Nearest neighbour bond	Bond type														
	Al-Al			Si-Al			Si-Si			Ge-Al			Si-Ge		
	1st	2nd	3rd												
$Ni_3Ge_{(1-x)}Si_x$															
Ni_3Ge	0	0	0	0	0	0	0	0	0	0	0	0	0	0	0
$Ni_3Ge_{0.875}Si_{0.125}$	0	0	0	0	0	0	0	0	0	0	0	0	0	6	12
$Ni_3Ge_{0.75}Si_{0.25}$	0	0	0	0	0	0	0	2	0	0	0	0	3	6	6
$Ni_3Ge_{0.75}Si_{0.25}-1$	0	0	0	0	0	0	0.5	0	0	0	0	0	2	6	4
$Ni_3Ge_{0.75}Si_{0.25}-2$	0	0	0	0	0	0	0	1	0	0	0	0	3	4	3
$Ni_3Ge_{0.625}Si_{0.375}$	0	0	0	0	0	0	0	3	0	0	0	0	4.5	3	6
$Ni_3Ge_{0.625}Si_{0.375}-1$	0	0	0	0	0	0	0.5	1	2	0	0	0	3.5	7	4
$Ni_3Ge_{0.625}Si_{0.375}-2$	0	0	0	0	0	0	1	0	0	0	0	0	3	7	4
$Ni_3Ge_{0.5}Si_{0.5}$	0	0	0	0	0	0	0	6	0	0	0	0	6	1.5	6
$Ni_3Ge_{0.5}Si_{0.5}-1$	0	0	0	0	0	0	1	2	4	0	0	0	4.5	3	6
$Ni_3Ge_{0.5}Si_{0.5}-2$	0	0	0	0	0	0	2	2	0	0	0	0	3.5	7	2
$Ni_3Ge_{0.5}Si_{0.5}-3$	0	0	0	0	0	0	1.5	3	0	0	0	0	2.5	7	4
$Ni_3Ge_{0.5}Si_{0.5}-4$	0	0	0	0	0	0	1.5	2	2	0	0	0	6	0	0
$Ni_3Ge_{0.5}Si_{0.5}-5$	0	0	0	0	0	0	2	2	0	0	0	0	4	1	2
$Ni_3Ge_{0.375}Si_{0.625}$	0	0	0	0	0	0	1.5	6	2	0	0	0	2	8	2
$Ni_3Ge_{0.375}Si_{0.625}-1$	0	0	0	0	0	0	2	4	4	0	0	0	8	0	0
$Ni_3Ge_{0.375}Si_{0.625}-2$	0	0	0	0	0	0	2.5	4	2	0	0	0	3	8	2
$Ni_3Ge_{0.25}Si_{0.75}$	0	0	0	0	0	0	3	6	6	0	0	0	2.5	7	2
$Ni_3Ge_{0.25}Si_{0.75}-1$	0	0	0	0	0	0	3.5	6	4	0	0	0	6	4	0
$Ni_3Ge_{0.25}Si_{0.75}-2$	0	0	0	0	0	0	3	7	4	0	0	0	3	4	0
$Ni_3Ge_{0.125}Si_{0.875}$	0	0	0	0	0	0	4.5	9	6	0	0	0	1.5	3	2

Table 12: Nine different DFT simulated elastic constants (in Gpa) for the compositions of $Ni_3Ge_{(1-x)}Si_x$

$Ni_3Ge_{(1-x)}Si_x$	C11	C22	C33	C12	C13	C23	C44	C55	C66
Ni_3Ge	269	269	269	147	147	147	105	105	105
$Ni_3Ge_{0.875}Si_{0.125}$	269	274	273	147	146	149	108	108	108
$Ni_3Ge_{0.75}Si_{0.25}$	284	279	286	153	156	154	111	111	111
$Ni_3Ge_{0.75}Si_{0.25}-1$	281	275	278	149	151	148	111	111	111
$Ni_3Ge_{0.75}Si_{0.25}-2$	279	267	268	144	145	140	111	111	111
$Ni_3Ge_{0.625}Si_{0.375}$	293	285	288	157	159	155	114	114	113
$Ni_3Ge_{0.625}Si_{0.375}-1$	287	284	281	155	153	151	114	114	114
$Ni_3Ge_{0.625}Si_{0.375}-2$	290	284	283	155	155	152	114	114	114
$Ni_3Ge_{0.5}Si_{0.5}$	288	287	288	154	154	154	117	117	117
$Ni_3Ge_{0.5}Si_{0.5}-1$	289	289	288	155	154	154	116	116	118
$Ni_3Ge_{0.5}Si_{0.5}-2$	283	289	289	152	152	154	117	117	117
$Ni_3Ge_{0.5}Si_{0.5}-3$	292	292	292	157	157	157	117	117	117
$Ni_3Ge_{0.5}Si_{0.5}-4$	282	283	288	149	151	152	116	117	116
$Ni_3Ge_{0.5}Si_{0.5}-5$	290	293	280	157	151	152	117	117	117
$Ni_3Ge_{0.375}Si_{0.625}$	292	297	293	158	156	158	120	120	120
$Ni_3Ge_{0.375}Si_{0.625}-1$	302	298	299	163	164	161	120	120	120
$Ni_3Ge_{0.375}Si_{0.625}-2$	292	295	295	156	156	157	120	120	120
$Ni_3Ge_{0.25}Si_{0.75}$	301	299	299	160	160	159	123	123	123
$Ni_3Ge_{0.25}Si_{0.75}-1$	309	287	299	158	163	153	123	123	123
$Ni_3Ge_{0.25}Si_{0.75}-2$	297	291	294	154	155	153	123	123	123
$Ni_3Ge_{0.125}Si_{0.875}$	299	303	300	158	156	158	126	126	126

5.1 Developing and interpreting neural networks using TensorFlow for result analysis.

- To establish a reliable predictive mapping between the coordination number technique (RDF) and the 9 C_{ij} constants, the training and testing datasets were divided, with approximately 50% to 90% of the data allocated for training and the remaining portion for testing. The hyperas optimization technique was employed to fine-tune the hyperparameters. Each individual hyperparameter was defined within a specific range: neurons varied from 1 to 100, layers ranged from 0 to 5, and activation functions including relu, sigmoid, tanh, and linear were considered as choices. The value of delta, used in the Huber loss function, was also tuned across the range of 0.1 to 50. Additionally, two types of regularizers, namely L1 and L2, were incorporated with respective regularization strengths ranging from 0 to 0.1. The optimizer function was selected within the hyperparameter space using if-elif conditions, with options including SGD, RMSprop, Adam, Adagrad, and Adamax, and their respective learning rates varied logarithmically from -6 to -3. The patience level, a hyperparameter condition controlling the number of epochs required to minimize the validation loss of the training set during cross-validation, was also fine-tuned. During each epoch or iteration, the weights between the input features (x) and output values (y) were updated using the backpropagation technique with the assistance of the optimizer. Once the optimal hyperparameters were generated, they were employed to train the best model.
- After determining the hyperparameters, the best model was evaluated using different training dataset sizes ranging from approximately 50% to 90%. However, the results presented here focus on the performance of the model using 75% and 50% training datasets. The ML-NN model exhibited varying performance across the training dataset sizes, with r^2 (root mean squared error) scores ranging from 0.65 to 0.85 on the unseen testing dataset. Additionally, the model was tested on its own training data to predict the results, revealing r^2 scores within the range of 0.6 to 0.78 for the aforementioned variation in training dataset sizes from 50% to 90%. MAE errors of both training and test set of 75% and 50% trained ML model are indicated in pair plot grid.
- The developed model demonstrates reliable prediction capability for the majority of cases in terms of DFT elastic constants. However, in specific instances such as the C_{12} constant, the performance is relatively poorer due to a limited number of training data points at the extreme ends of the Gpa scale. This issue could potentially be addressed by selectively adding more training data points within that range. Nonetheless, considering that the ML model was trained on only 63 data points with 18 input features and 9 output features, the achieved performance is remarkable.

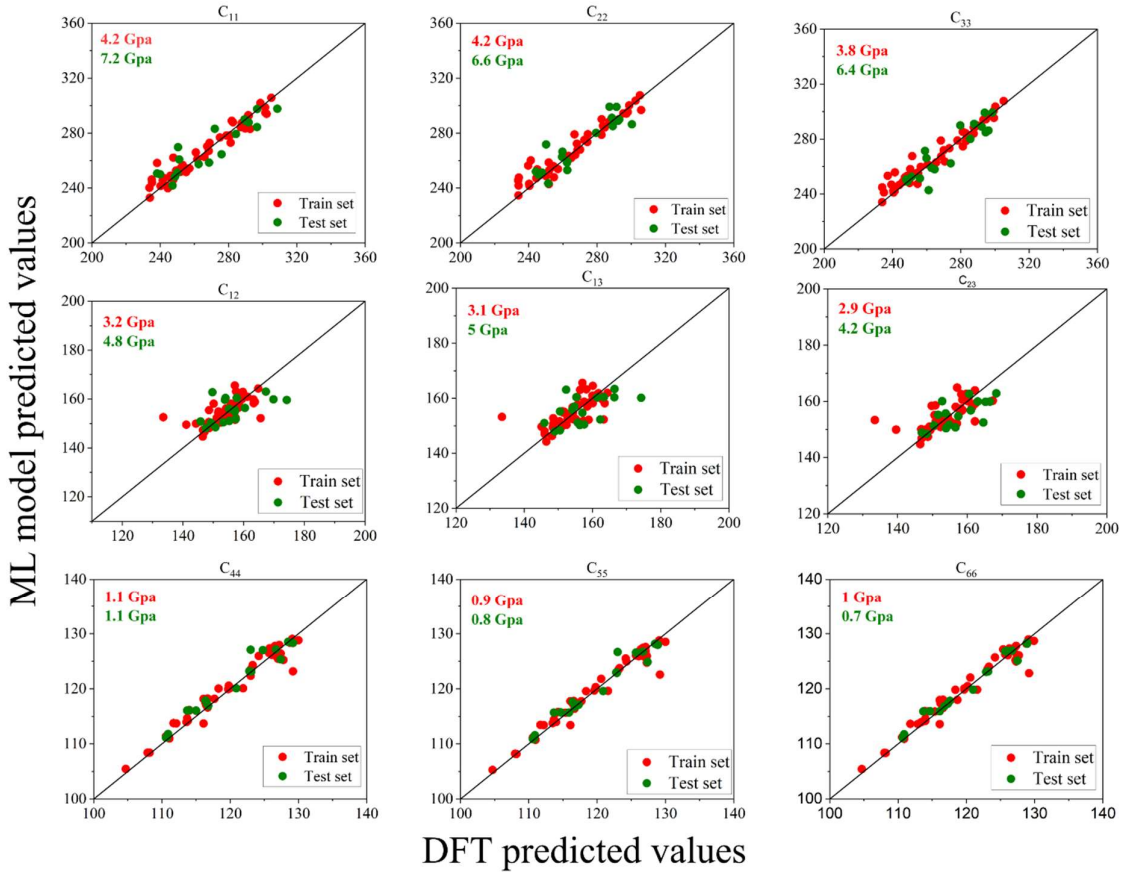


Figure 14: Pair plot grid comparing the C_{ij} constants predicted by the neural networks model against the ones calculated using DFT. The training and test sets consisted of 75% and 25% of the data respectively.

- The training and testing datasets mentioned in the above figures consist of an equal amount of data from all three alloy systems: $\text{Ni}_3\text{Al}_{(1-x)}\text{Ge}_x$, $\text{Ni}_3\text{Ge}_{(1-x)}\text{Si}_x$ and $\text{Ni}_3\text{Si}_{(1-x)}\text{Ge}_x$.
- The numbers on the top left corner of each plot represent the mean absolute error (MAE) values for the training and test sets indicating the overall error with respect to DFT values.

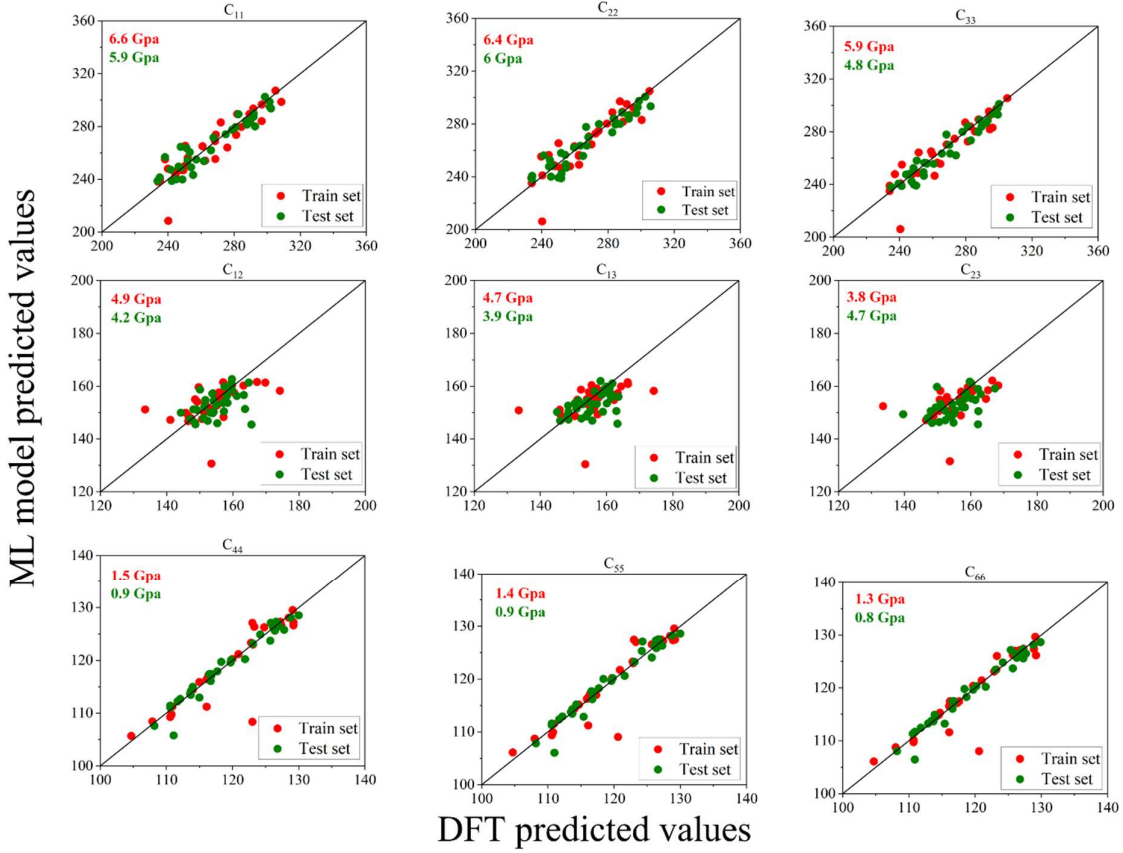


Figure 15: Pair plot grid comparing the C_{ij} constants predicted by the neural networks model against the ones calculated using DFT. The training and test sets consisted of 50% and 50% of the data respectively.

- The training and testing datasets mentioned in the above figures consist of an equal amount of data from all three alloy systems: $\text{Ni}_3\text{Al}_{(1-x)}\text{Ge}_x$, $\text{Ni}_3\text{Ge}_{(1-x)}\text{Si}_x$ and $\text{Ni}_3\text{Si}_{(1-x)}\text{Ge}_x$.
- The numbers on the top left corner of each plot represent the mean absolute error (MAE) values for the training and test sets indicating the overall error with respect to DFT values.
- It is observed that the configurations with larger disparities between DFT-predicted and ML-predicted errors tend to correspond to those with higher least square fit errors in the DFT simulations. In the order to maintain strain below 5% while predicting the elastic constants of $\text{Ni}_3\text{Al}_{(1-x)}\text{Ge}_x$, $\text{Ni}_3\text{Al}_{(1-x)}\text{Si}_x$, $\text{Ni}_3\text{Ge}_{(1-x)}\text{Si}_x$ systems , three different strains of about 0.12%, 0.24%, 0.36% are imposed. However, using these strains for the lesser weightage compositional configurations led to increase in least square fitting errors when calculating stress and correlating it to obtain elastic constants. To address this issue, VASP manual suggests employing strains around 2% for accurate DFT predictions for the lesser weightage compositional configurations.

- And also, these compositional configurations with higher least square fit errors have a lesser weightage in determining the overall composition values. Therefore, when plotting the overall composition values, there will be no significant change in the observed trends. However, when developing the ML model, the weightage of configurations is not considered as an input variable. Instead, the focus is solely on mapping the structural descriptors to the output values. Due to this constraint, these configurations are treated as outliers and are not trained effectively, leading to poor performance on the testing set if any structural configuration in the testing set resembles the mentioned training set configuration. And these seen in the case of certain configurations for the values of C_{12} elastic constants.
- To address this issue, I have made changes to the strain values, adjusting them to around 2%, and calculated stress and correlating to obtain changes in elastic constants ,and it is observed a reduction in the least square fit errors. This makes the improvement in results of ML model further. It is important to note that deviations in the trends of C_{12} 's elastic constants are only because of these lesser-weighted compositional configurations which exhibits lesser stability, as they tend to behave differently in terms of the output elastic values when strain values are altered, which should not occur.
- When altering the strain values in the lesser-weighted configurations, it was observed that the averaged values of the 9 elastic constants, which are further condensed into 3 elastic constants, remained constant. As a result, the overall composition value also remained the same, with the weighted averaged value of the configurations contributing to the composition. However, the individual values of the 9 elastic constants showed reduced deviations and became more evenly distributed.
- This even distribution of the elastic constants has proven beneficial for training the ML model, as it allows for better performance and improved results on unseen test data. By achieving a more balanced representation of the elastic constants, the model can effectively capture the relationships between the structural descriptors and the output values, leading to enhanced predictive capabilities.

Chapter 6

Validation the developed neural networks model

6.1 Validating on intermediate compositions of ternary phase diagram of $\text{Ni}_3\text{Al}_{(1-x-y)}\text{Ge}_x\text{Si}_y$

- Using the previously established procedure, the first three nearest neighbours of bond types of Al-Al, Al-Ge, Al-Si, Ge-Ge, Ge-Si, and Si-Si were calculated in the alloy compositions $\text{Ni}_3\text{Al}_{(1-x-y)}\text{Ge}_x\text{Si}_y$. These calculations generate descriptors for the compositions, which were then used as the x-input features for the developed model. The model, trained on the configurations of all compositions along the line of the ternary phase diagram of $\text{Ni}_3\text{Al}_{(1-x-y)}\text{Ge}_x\text{Si}_y$ produce results based on the given x-input features.
- The ML-Neural network predicted output features were compared with the DFT predicted output features for 15 configurations, as reported in the tables below. It was observed that the ML predicted values were more or less within an error margin of 5% compared to the DFT values. Therefore, the model developed on the pseudo-binary configurations effectively functions for the pseudo-ternary systems.

Table 13: 15 different compositional configurations of Nickel-based pseudo-ternary alloys on which NN model is validated.

1	$\text{Ni}_3\text{Al}_{0.725}\text{Ge}_{0.125}\text{Si}_{0.125}$
2	$\text{Ni}_3\text{Al}_{0.725}\text{Ge}_{0.125}\text{Si}_{0.125}-1$
3	$\text{Ni}_3\text{Al}_{0.725}\text{Ge}_{0.125}\text{Si}_{0.125}-2$
4	$\text{Ni}_3\text{Al}_{0.25}\text{Ge}_{0.375}\text{Si}_{0.375}$
5	$\text{Ni}_3\text{Al}_{0.25}\text{Ge}_{0.375}\text{Si}_{0.375}-1$
6	$\text{Ni}_3\text{Al}_{0.25}\text{Ge}_{0.375}\text{Si}_{0.375}-2$
7	$\text{Ni}_3\text{Al}_{0.25}\text{Ge}_{0.375}\text{Si}_{0.375}-3$
8	$\text{Ni}_3\text{Al}_{0.375}\text{Ge}_{0.375}\text{Si}_{0.25}$
9	$\text{Ni}_3\text{Al}_{0.375}\text{Ge}_{0.375}\text{Si}_{0.25}-1$
10	$\text{Ni}_3\text{Al}_{0.375}\text{Ge}_{0.375}\text{Si}_{0.25}-2$
11	$\text{Ni}_3\text{Al}_{0.375}\text{Ge}_{0.375}\text{Si}_{0.25}-3$
12	$\text{Ni}_3\text{Al}_{0.25}\text{Ge}_{0.5}\text{Si}_{0.25}$
13	$\text{Ni}_3\text{Al}_{0.25}\text{Ge}_{0.5}\text{Si}_{0.25}-1$
14	$\text{Ni}_3\text{Al}_{0.25}\text{Ge}_{0.5}\text{Si}_{0.25}-2$
15	$\text{Ni}_3\text{Al}_{0.25}\text{Ge}_{0.5}\text{Si}_{0.25}-3$

Table 14: Comparison of DFT simulated and ML model predicted 9 different elastic constants(in Gpa) with margin of errors for compositional configurations of $Ni_3Al_{0.725}Ge_{0.125}Si_{0.125}$

Ni₃Al_{0.725}Ge_{0.125}Si_{0.125}	DFT predicted (Gpa)	ML predicted (Gpa)	Error(%)
C ₁₁	243.3	246.8	1.4
C ₂₂	231.7	249.3	7.6
C ₃₃	243.6	247	1.4
C ₁₂	152	156.9	3.2
C ₁₃	158.1	157.5	0.4
C ₂₃	152.1	153.6	0.9
C ₄₄	122.4	125.5	2.5
C ₅₅	122.4	125.6	2.6
C ₆₆	122.4	125.7	2.7
Ni₃Al_{0.725}Ge_{0.125}Si_{0.125}- 1	DFT predicted (Gpa)	ML predicted (Gpa)	Error(%)
C ₁₁	237.2	243.4	2.6
C ₂₂	239.1	246.6	3.1
C ₃₃	238.5	245.2	2.8
C ₁₂	156.4	156.5	0.06
C ₁₃	157.4	156.6	0.5
C ₂₃	157.8	160.7	1.8
C ₄₄	121.7	124.6	2.4
C ₅₅	121.7	124.8	2.5
C ₆₆	121.9	124.8	2.4
Ni₃Al_{0.725}Ge_{0.125}Si_{0.125}- 2	DFT predicted (Gpa)	ML predicted (Gpa)	Error(%)
C ₁₁	240.4	243.3	1.2
C ₂₂	242.2	251.5	3.8
C ₃₃	240.2	245.2	2.1
C ₁₂	157.1	156.8	0.2
C ₁₃	156.1	157.5	0.9
C ₂₃	159	161	1.3
C ₄₄	122.2	124.8	2.1
C ₅₅	121.5	125.1	2.9
C ₆₆	121.5	125.1	2.9

Table 15: Comparison of DFT simulated and ML model predicted 9 different elastic constants(in Gpa) with margin of errors for compositional configurations of $Ni_3Al_{0.25}Ge_{0.375}Si_{0.375}$

$Ni_3Al_{0.25}Ge_{0.375}Si_{0.375}$	DFT predicted (Gpa)	ML predicted (Gpa)	Error(%)
C ₁₁	272	273.4	0.5
C ₂₂	285.1	276.8	2.9
C ₃₃	261.8	274.6	4.9
C ₁₂	157.4	156.6	0.5
C ₁₃	145.6	158.6	8.9
C ₂₃	152.16	158.5	4.2
C ₄₄	119	119.7	0.5
C ₅₅	119.1	119.9	0.6
C ₆₆	119.2	119.9	0.6
$Ni_3Al_{0.25}Ge_{0.375}Si_{0.375}-1$	DFT predicted (Gpa)	ML predicted (Gpa)	Error(%)
C ₁₁	270.2	269.8	0.1
C ₂₂	289.6	272.1	6
C ₃₃	286.2	272.7	4.7
C ₁₂	158.4	157.6	0.5
C ₁₃	157.4	159.1	1.1
C ₂₃	166.7	159.1	4.6
C ₄₄	118.8	119.2	0.3
C ₅₅	118.8	119.3	0.4
C ₆₆	118.9	119.6	0.6
$Ni_3Al_{0.25}Ge_{0.375}Si_{0.375}-2$	DFT predicted (Gpa)	ML predicted (Gpa)	Error(%)
C ₁₁	289.7	269.9	6.8
C ₂₂	261.2	273.3	4.6
C ₃₃	260.2	272.3	4.8
C ₁₂	153.2	156.5	2.2
C ₁₃	152.8	158.6	3.8
C ₂₃	140.3	158.4	12
C ₄₄	119.6	119.1	0.4
C ₅₅	119.3	119.3	0
C ₆₆	119.3	119.2	0.08
$Ni_3Al_{0.25}Ge_{0.375}Si_{0.375}-3$	DFT predicted (Gpa)	ML predicted (Gpa)	Error(%)
C ₁₁	277.1	268.9	2.9
C ₂₂	275.8	271.4	1.6
C ₃₃	276.3	270.5	2.1
C ₁₂	155.3	156.3	0.6
C ₁₃	155.6	157.8	1.4
C ₂₃	153.7	157.9	2.7
C ₄₄	119.3	118.8	0.4
C ₅₅	118.7	118.9	0.2
C ₆₆	118.5	118.9	0.3

Table 16: Comparison of DFT simulated and ML model predicted 9 different elastic constants(in Gpa) with margin of errors for compositional configurations of $Ni_3Al_{0.375}Ge_{0.375}Si_{0.25}$

Ni₃Al_{0.375}Ge_{0.375}Si_{0.25}	DFT predicted (Gpa)	ML predicted (Gpa)	Error(%)
C ₁₁	263.6	263.6	0
C ₂₂	262.7	267.3	1.8
C ₃₃	261.2	265.3	1.6
C ₁₂	153.2	156.3	2
C ₁₃	151.8	159.1	4.8
C ₂₃	152.1	158.2	4
C ₄₄	117.2	118.6	1.2
C ₅₅	117.5	118.9	1.2
C ₆₆	117.9	118.9	0.8
Ni₃Al_{0.375}Ge_{0.375}Si_{0.25-1}	DFT predicted (Gpa)	ML predicted (Gpa)	Error(%)
C ₁₁	262.9	263.2	0.1
C ₂₂	258	268.2	3.4
C ₃₃	263	264	0.4
C ₁₂	152.4	155.8	2.2
C ₁₃	152.9	158.1	3.4
C ₂₃	151.5	158.3	4.5
C ₄₄	116.4	119.2	2.4
C ₅₅	116.4	119.5	2.7
C ₆₆	117.7	119.5	1.5
Ni₃Al_{0.375}Ge_{0.375}Si_{0.25-2}	DFT predicted (Gpa)	ML predicted (Gpa)	Error(%)
C ₁₁	258.7	260.9	0.8
C ₂₂	258.9	265.5	2.5
C ₃₃	259.3	262.2	1.1
C ₁₂	154.7	155.1	0.3
C ₁₃	154	156.3	1.5
C ₂₃	155.1	157.5	1.6
C ₄₄	116.9	118.3	1.2
C ₅₅	117.8	118.6	0.7
C ₆₆	117.6	118.5	0.8
Ni₃Al_{0.375}Ge_{0.375}Si_{0.25-3}	DFT predicted (Gpa)	ML predicted (Gpa)	Error(%)
C ₁₁	270.3	259.7	3.9
C ₂₂	264.6	264.7	0.03
C ₃₃	263.8	261.9	0.7
C ₁₂	155.8	155.8	0
C ₁₃	157.8	158.1	0.2
C ₂₃	154.1	158.3	2.7
C ₄₄	118.6	118.6	0
C ₅₅	117.7	118.9	1
C ₆₆	117.6	118.8	1

Table 17: Comparison of DFT simulated and ML model predicted 9 different elastic constants(in Gpa) with margin of errors for compositional configurations of $Ni_3Al_{0.25}Ge_{0.5}Si_{0.25}$

$Ni_3Al_{0.25}Ge_{0.5}Si_{0.25}$	DFT predicted (Gpa)	ML predicted (Gpa)	Error(%)
C₁₁	267.9	271.9	1.5
C₂₂	269.5	273.1	1.3
C₃₃	270.5	270.3	0.07
C₁₂	151.5	155.9	2.9
C₁₃	152	157.8	3.8
C₂₃	150.6	156.7	4.1
C₄₄	114.6	116.8	1.9
C₅₅	115.7	117	1.1
C₆₆	115.9	117.6	1.5
$Ni_3Al_{0.25}Ge_{0.5}Si_{0.25-1}$	DFT predicted (Gpa)	ML predicted (Gpa)	Error(%)
C₁₁	270.2	271.9	0.6
C₂₂	272.9	273.1	0.07
C₃₃	267.4	270.3	1.1
C₁₂	153.8	155.9	1.4
C₁₃	152.7	157.8	3.3
C₂₃	154.1	156.7	1.7
C₄₄	115.8	116.9	0.9
C₅₅	115.9	117.1	1
C₆₆	114.5	117.7	2.8
$Ni_3Al_{0.25}Ge_{0.5}Si_{0.25-2}$	DFT predicted (Gpa)	ML predicted (Gpa)	Error(%)
C₁₁	271.4	267.9	1.3
C₂₂	269.9	269.8	0.03
C₃₃	268.8	269.9	0.4
C₁₂	150.3	156.5	4.1
C₁₃	150.3	158.9	5.7
C₂₃	150	157.9	5.2
C₄₄	116	116.7	0.6
C₅₅	116	116.9	0.7
C₆₆	115.8	117.4	1.4
$Ni_3Al_{0.25}Ge_{0.5}Si_{0.25-3}$	DFT predicted (Gpa)	ML predicted (Gpa)	Error(%)
C₁₁	272.6	266.9	2.1
C₂₂	273.1	268.8	1.6
C₃₃	275.7	268.9	2.5
C₁₂	155.2	156.3	0.7
C₁₃	155.9	158	1.3
C₂₃	156.1	157.7	1
C₄₄	116.1	116.5	0.3
C₅₅	116.1	116.6	0.4
C₆₆	115.8	117.1	1.1

Chapter 7

Conclusion

- In the scope of this research, we conducted extensive calculations to determine the DFT-computed elastic constants for a total of 63 different configurations within the $\text{Ni}_3\text{Al}_{(1-x)}\text{Ge}_x$, $\text{Ni}_3\text{Ge}_{(1-x)}\text{Si}_x$ and $\text{Ni}_3\text{Si}_{(1-x)}\text{Ge}_x$ alloy systems. To capture the structural characteristics of these configurations, we employed the concept of nearest neighbour bonds, which allowed us to generate relevant structural descriptors.
- With the structural descriptors in hand, we proceeded to develop a machine learning (ML) model specifically tailored for predicting elastic properties. This ML model was trained using the available data on the aforementioned configurations, allowing it to learn the complex relationships between the structural descriptors and the corresponding elastic constants. By harnessing the power of ML, our model aimed to provide efficient and accurate predictions of the elastic properties of new configurations within these alloy systems.
- To ensure the reliability and robustness of the developed model, we subjected it to rigorous validation. This validation process involved testing the model's performance on pseudo-ternary systems, which expanded the applicability of the model beyond the initial pseudo-binary systems. By evaluating the model's predictions against the DFT-computed elastic constants for a set of pseudo-ternary configurations, we assessed its ability to generalize and accurately predict elastic properties in new contexts.
- Finally, to highlight the practical implications of our developed model, we applied it to make high-throughput predictions. By leveraging the model's capabilities, we were able to swiftly and accurately predict the elastic properties of all possible ternary phase compositions within the studied alloy systems. This demonstration showcased the potential of our model to expedite material screening and exploration, providing valuable insights for the design and development of new alloy compositions with desired elastic properties.

References

- 1.Batra, R., Tran, H. D., Kim, C., Chapman, J., Chen, L., Chandrasekaran, A., & Ramprasad, R. (2019). General Atomic Neighborhood Fingerprint for Machine Learning-Based Methods. *Journal of physical chemistry C*. <https://doi.org/10.1021/acs.jpcc.9b03925>
- 2.Huang, M. L., & Wang, C. Y. (2016a). First-principles studies of effects of interstitial boron and carbon on the structural, elastic, and electronic properties of Ni solution and Ni₃Al intermetallics. *Chinese Physics B*, 25(10). <https://doi.org/10.1088/1674-1056/25/10/107104>
- 3.Huang, M. L., & Wang, C. Y. (2016b). First-principles studies of effects of interstitial boron and carbon on the structural, elastic, and electronic properties of Ni solution and Ni₃Al intermetallics. *Chinese Physics B*, 25(10). <https://doi.org/10.1088/1674-1056/25/10/107104>
- 4.Jgilman, J. (n.d.). Electronic basis of the strength of the materials.
- 5.Kim, D. E., Shang, S. L., & Liu, Z. K. (2010). Effects of alloying elements on elastic properties of Ni₃Al by first-principles calculations. *Intermetallics*, 18(6), 1163–1171. <https://doi.org/10.1016/j.intermet.2010.02.024>
- 6.Lang, N. D., & Kohn, W. (1970). Theory of Metal Surfaces: Charge Density and Surface Energy~. In *physical review* (Vol. 8).
- 7.Luan, X., Qin, H., Liu, F., Dai, Z., Yi, Y., & Li, Q. (2018). The mechanical properties and elastic anisotropies of cubic Ni₃Al from first principles calculations. *Crystals*, 8(8). <https://doi.org/10.3390/crust8080307>
- 8.Ramprasad, R., Batra, R., Pilania, G., Mannodi-Kanakkithodi, A., & Kim, C. (2017). Machine learning in materials informatics: Recent applications and prospects. In *npj Computational Materials* (Vol. 3, Issue 1). Nature Publishing Group. <https://doi.org/10.1038/s41524-017-0056-5>
- 9.Revi, V., Kasodariya, S., Talapatra, A., Pilania, G., & Alankar, A. (2021). Machine learning elastic constants of multi-component alloys. *Computational Materials Science*, 198. <https://doi.org/10.1016/j.commatsci.2021.110671>
- 10.Rose, J. H., & Shore, H. B. (1990). Bonding energetics of metals: Explanation of trends (Vol. 43).
- 11.Rose', J. H., & Shore~, H. B. (1994). Elastic constants of the transition metals from a uniform electron gas (Vol. 49).
- 12.Shang, S. L., Wang, Y., Kim, D. E., & Liu, Z. K. (2010). First-principles thermodynamics from phonon and Debye model: Application to Ni and Ni₃Al. *Computational Materials Science*, 47(4), 1040–1048. <https://doi.org/10.1016/j.commatsci.2009.12.006>
- 13.Ueda, M., Yasuda, H., Umakoshi, Y., Wang, S., Xu, L., Tong, J., Miedema, A. R., De Boer, F. R., & De Chatel, P. F. (1973). Empirical description of the role of

- electronegativity in alloy formation Investigation into convective heat transfer of nanofluids at the thermal boundary layer development region in micro-channels Empirical description of the role of electronegativity in alloy formation. In Journal of Physics F: Metal Physics J. Phys. F: Metal Phys (Vol. 3).
14. Wang, J., Du, Y., Shang, S. L., Liu, Z. K., & Li, Y. W. (2014). Effects of alloying elements on elastic properties of Al by first-principles calculations. *Journal of Mining and Metallurgy, Section B: Metallurgy*, 50(1), 37–44.
<https://doi.org/10.2298/JMMB140116002W>
15. Wen, M., & Wang, C. Y. (2018). Transition-metal alloying of γ' -Ni₃Al: Effects on the ideal uniaxial compressive strength from first-principles calculations. *Physical Review B*, 97(2). <https://doi.org/10.1103/PhysRevB.97.024101>
16. Wu, Q., & Li, S. (2012a). Alloying element additions to Ni 3Al: Site preferences and effects on elastic properties from first-principles calculations. *Computational Materials Science*, 53(1), 436–443. <https://doi.org/10.1016/j.commatsci.2011.09.016>
17. Wu, Q., & Li, S. (2012b). Alloying element additions to Ni 3Al: Site preferences and effects on elastic properties from first-principles calculations. *Computational Materials Science*, 53(1), 436–443. <https://doi.org/10.1016/j.commatsci.2011.09.016>
18. Sholl DS, Steckel JA, Density Functional Theory, John Wiley & Sons, Hoboken,NJ,USA,2009.

Appendix

Optimization

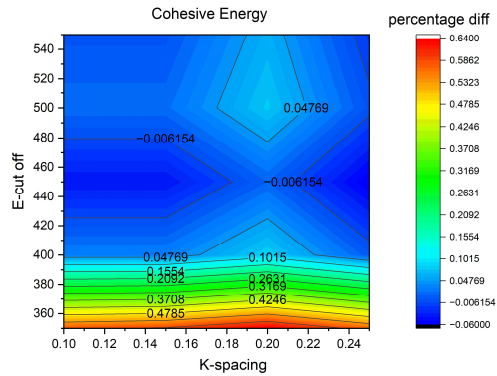


Figure 16: Contour plot comparing convergence of E-cut off vs K-spacing for the optimal cohesive energy of relaxed volume of Ni₃Al

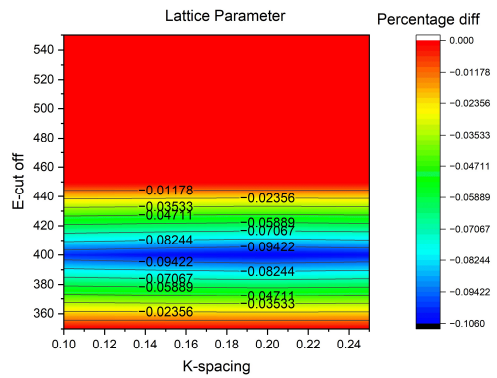


Figure 17: Contour plot comparing convergence of E-cut off vs K-spacing for the optimal lattice parameter of relaxed volume of Ni₃Al

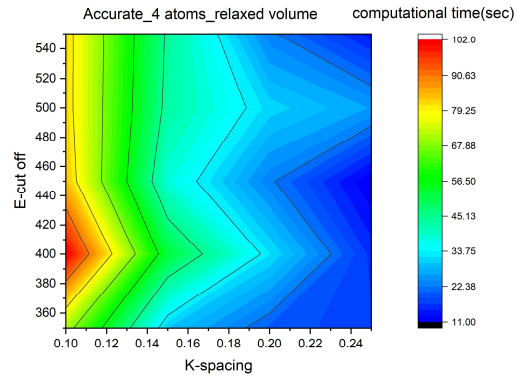


Figure 18: Contour plot comparing convergence of E-cut off vs K-spacing for the optimal computational time of relaxed volume of Ni₃Al

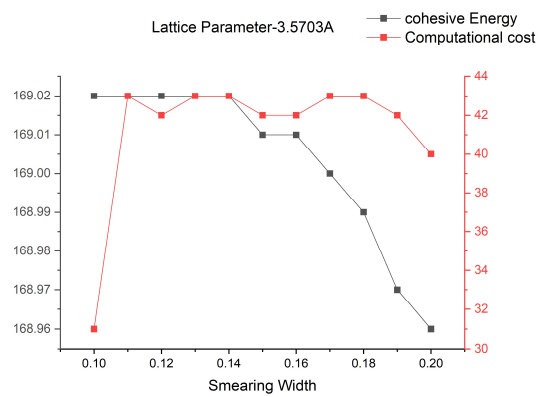


Figure 19: line plot comparing smearing width convergence w.r.t to cohesive energy and computational cost of Ni₃Al